

TECHNICAL AND RESEARCH BULLETIN NO. 1-45 (2022)

GUIDE FOR CFD-INFORMED AUV MANEUVERING MODELS

Prepared by

**VIRGINIA TECH
CENTER FOR MARINE AUTONOMY AND ROBOTICS**

Authors
Taylor Njaka Stefano Brizzolara Daniel J. Stilwell

Editor
**Adrian S. Onas
WEBB INSTITUTE**

January 5, 2022



Published by

The Society of Naval Architects and Marine Engineers

99 Canal Center Plaza, Alexandria, VA 22314 USA

Copyright 2021 by the Society of Naval Architects and Maritime Engineers with rights reserved.

TABLE OF CONTENTS

TABLE OF CONTENTS	i
ABSTRACT	ii
1 INTRODUCTION	1
2 COORDINATE SYSTEMS	3
3 FIN ANGLE SIGN CONVENTION	4
3.1 Implementation of Traditional Rudder Commands onto Rear Fins	4
3.2 Basic Rudder Command Roll Compensation (as Opposed to Roll Control)	4
3.3 Roll Control	5
3.4 Control-Command Superposition on Rear Fins	6
3.5 Reconstructing δ_r , δ_e , and δ_{roll} from Clipped Fin Angles for Control Force Estimation	7
3.6 Generic Approach to Control-Command Implementation	8
4 KINEMATICS	9
5 DYNAMICS	10
5.1 Mass and Payload Distribution	10
5.2 Rigid-body Dynamics	10
5.3 Added Inertia Dynamics	11
5.4 Hydrodynamic damping	11
5.5 Gravitational Restoring Forces and Moments	12
5.6 Control Forces and Moments	12
5.7 Final Update Laws	12
6 HYDRODYNAMIC COEFFICIENTS ESTIMATION	13
6.1 Estimation of Hull Coefficients	13
6.1.1 Pure-Sway	14
6.1.2 Pure-Yaw	16
6.1.3 Pure-Surge	16
6.1.4 VPMM Computational Setup	17
6.2 Estimation of Rudder Control Surface Coefficients	17
6.3 Vertical Plane (Pitch-Axis) Coefficients	18
6.3.1 Pitch-Axis Hull Coefficients	18
6.3.2 Elevator Control Surface Coefficients	19
6.3.3 Canard Control Surface Coefficients	19
6.4 Roll Coefficients	19
6.4.1 Estimation of Control Surface Roll Coefficient $K_{uu\delta roll}$	19
6.4.2 Estimation of Hull Coefficients K_{up} , K_{pp} , and $K_{\dot{p}}$	20
7 6-DOF MODEL SIMULATION AND CONSTRUCTION	21
7.1 Open-Loop Simulation	21
7.2 Closed-Loop Simulation	21
8 Accuracy Assessment Using VT-690 AUV CFD Trajectory	23
8.1 Full CFD Turning-Circle Model	23
8.2 6-DOF Model Trajectory Comparison	23
9 CONCLUSION	25
SYMBOLS AND ABBREVIATIONS	26
REFERENCES	29

ABSTRACT

In this report, we propose and detail a comprehensive theory and numerical implementation of a six degree of freedom (6-DOF) dynamic AUV model utilizing CFD and first principles, providing a systematic approach to accurately estimate all parameters required for maneuvering. Possible simplifications and methodologies for different AUV profiles are covered, rendering the study applicable to any torpedo-profiled underwater vehicle that uses control surfaces to maneuver. Potential redundancies between added-Coriolis and hydrodynamic damping terms in the literature are also clarified in this study. Coordinate systems are discussed, and the physical implementation of control-commands (for roll, pitch, and yaw) onto various sets of control surfaces is detailed. The implementation of all hydrodynamic terms is then covered, followed by coefficient estimation using CFD Planar Motion Mechanism tests and other methods. A final nonlinear 6-DoF model is presented both with and without feedback, for which model performance is evaluated using a known AUV and a fully-conceptual AUV. This paper is intended to serve as a complete guide to control and simulate any AUV to a high degree of accuracy.

1. INTRODUCTION

Since the inception of Computational Fluid Dynamics (CFD), the estimation of traditional hydrodynamic coefficients for underwater vehicle maneuvering models has been largely facilitated, yet the fundamental principals remain unchanged. Traditionally, to derive such coefficients, a physical craft would be embedded with two rods and forced on a sinusoidal path inside a towing tank. Forces were measured between the rods to determine the relative hydrodynamic forces and moments at the craft's center of buoyancy [11]. These original test maneuvers would provide information regarding how hydrodynamic forces relate to velocity components on a planar trajectory, greatly simplifying the estimation of hydrodynamic coefficients. The tests were appropriately referred to as Planar-Motion Mechanism (PMM) tests. In the modern age, when a physical PMM test setup is actually feasible, every hydrodynamic coefficient can be accurately estimated experimentally [15, 12]. Typically, modern PMMs are instead conducted *virtually* in CFD by summing the hydrodynamic force contributions of millions of virtual cells touching the AUV body during its forced planar trajectory. These CFD simulations are known as Virtual PMM (VPMM) tests. Both PMMs and VPMMs utilize planar trajectories to simplify the dynamic EOM and facilitate coefficient estimation and can accurately measure added-mass and damping coefficients simultaneously.

However, some modern studies utilize CFD only to estimate hydrodynamic damping coefficients through virtual steady-drift tests, while relying somewhat on geometric ellipsoidal approximations for nearly all added-mass terms [20, 10, 5, 8]. One study [9] uses an accelerating linear flow in a quasi-steady RANS CFD setup in conjunction with geometric approximations to calculate added-mass terms. The rationale behind avoiding VPMM tests is justified through "ambiguities in the oscillatory motions that need to be dealt with" which our study aims to fully clarify. Another possible motive to avoid VPMM simulations stems from the considerable simplification of CFD computational setups without the use of unsteady moving meshes. However, with the ever-increasing performance of computational hardware, much more accurate models can and should be constructed utilizing fully-unsteady CFD solvers [13, 14, 19, 2]. The use of geometric approximations for all added-mass coefficients inherently invites error. It is no longer impractical to run VPMM tests on a craft and avoid approximating the hull as some equivalent ellipsoid for added-mass terms.

As such, our study thoroughly details the entire process of accurately modeling AUVs in the modern age, utilizing CFD and first principles. This paper thoroughly details the construction of a 6-DOF dynamic AUV model, and covers various coefficient identification methods with the rationale behind possible simplifications for different AUV profiles. We also aim to quell confusion regarding the implementation of traditional damping terms, as the relative novelty of CFD causes common misconceptions on redundancies in added-Coriolis terms that are only apparent if constructing a complete model from first principles. Coordinate systems are discussed, followed by actuator angle convention and command implementation onto control surfaces. Roll control is also discussed. A kinematic model is presented with the estimation of hydrodynamic terms through CFD and other methods. Least squares regression techniques are used for estimating nonlinear coefficients from VPMM datasets. The six-DOF model is then constructed from the final update laws with and without feedback. The model is ultimately validated through trajectory comparison with CFD using a known AUV, and a large theoretical AUV. Both AUVs are designed to cruise at at 4 knots. The known AUV is detailed in Table 1.1:

Table 1.1 – PHYSICAL AND PERFORMANCE PARAMETERS OF THE VT-690 AUV.

Parameter	Specification
Length	2.23 m
Diameter	17.5 cm
Displacement	43.0 kg
Endurance	24 hours @ 4 knots with all sensors operating
Max. depth	500 meters
Navigation	DVL and FOG IMU, acoustic ranging
Mission sensor	side-scan and bathymetric sonar
Communication	900 MHz RF modem, 802.11(WiFi), Iridium satcom, acoustic modem

The VT-690 AUV was developed by the Center for Marine Autonomy and Robotics at Virginia Tech. The vehicle does not possess front canards and has four rear control surfaces arranged in a T-tail configuration, shown in Figure 1.1.



Figure 1.1 – VIRGINA TECH 690 AUV, DEVELOPED AT THE CENTER FOR MARINE AUTONOMY AND ROBOTICS.

A fully-theoretical large X-tail AUV is also presented, and is detailed in Table 1.2.

Table 1.2 – PHYSICAL AND PERFORMANCE PARAMETERS OF THE FULLY-VIRTUAL CONCEPT AUV.

Parameter	Specification
Length	5.5 m
Diameter	0.71 m
Displacement	1831 kg
I_{zz}	3406 kg-m ²
Control-surface to hull-surface area-ratio	4.16%

The large Concept-AUV also does not possess front canards, but has four rear control surfaces arranged in an X-tail configuration, shown in Figure 1.2.

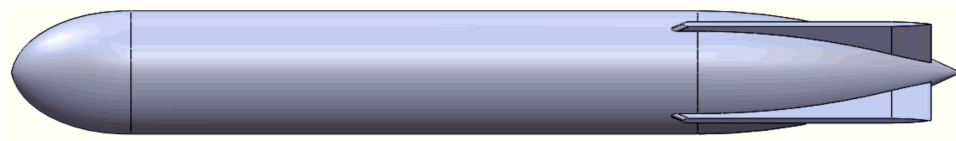


Figure 1.2 – LARGE THEORETICAL X-TAIL CONCEPT AUV.

The 6-DOF maneuvering model and methods detailed in this study are not tailored for the VT-690 AUV or the large Concept AUV. They are intended to be directly applicable to any torpedo-profiled underwater vehicle with any number of actuated control surfaces in any configuration. This study is intended to serve as a guide for constructing a 6-DOF model for any roughly-symmetrical AUV.

2. COORDINATE SYSTEMS

We adopt the typical right-handed convention for Cartesian coordinate systems and vehicle states. The linear velocity of the AUV is denoted by surge u , sway v , and heave w with respect to a body-fixed coordinate system show in Figure 2.1. The location of the origin of the body-fixed coordinate system with respect to a world coordinate system is denoted $\{x, y, z\}$. The orientation of the body-fixed coordinate systems with respect to the world coordinate system is represented by the Euler angles $\{\phi, \theta, \psi\}$. Body rotation rates are expressed with respect to the body coordinate system by $\{p, q, r\}$.

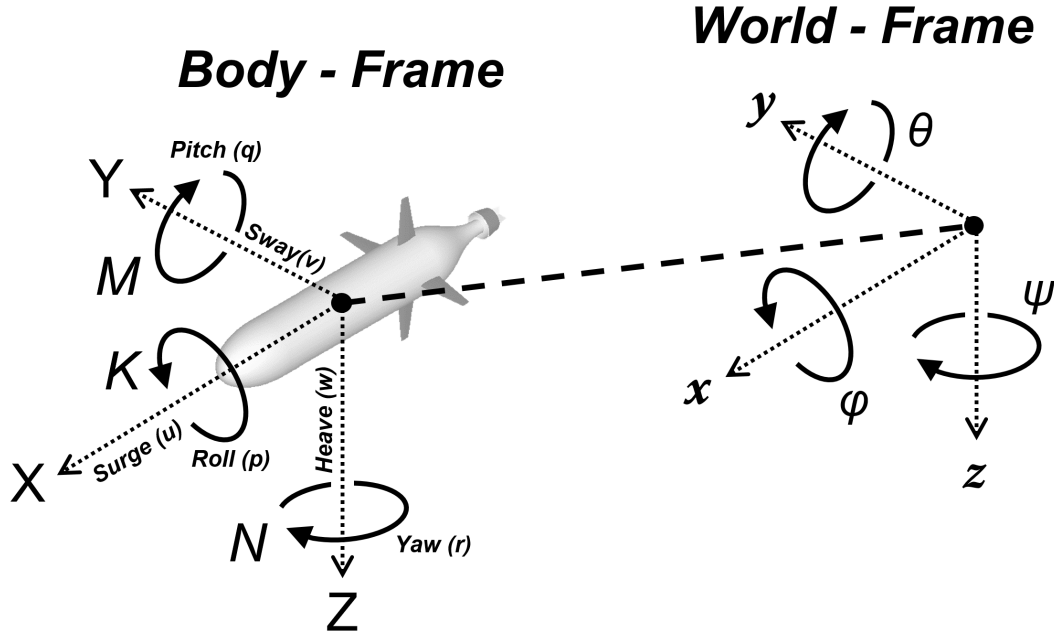


Figure 2.1 – COORDINATE SYSTEMS.

The rudder angle δ_r is shown in the top-down view of an AUV in Figure 2.2. A positive rudder command generates negative yaw moment and positive side-slip angle β .

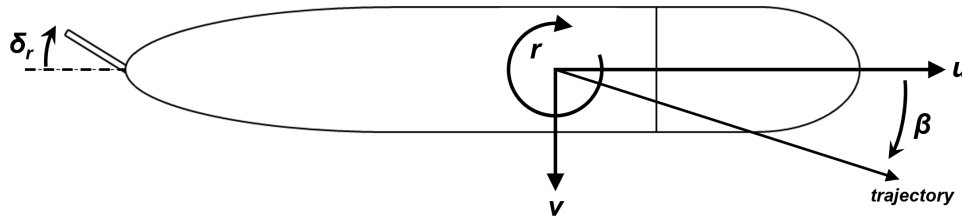


Figure 2.2 – TOP VIEW OF A GENERIC AUV BODY.

The elevator angle δ_e and canard angle δ_c are shown from the starboard-side view of an AUV in Figure 2.3. A positive elevator command generates positive pitch moment M and positive angle of attack α . Positive canard angle δ_c does the same.

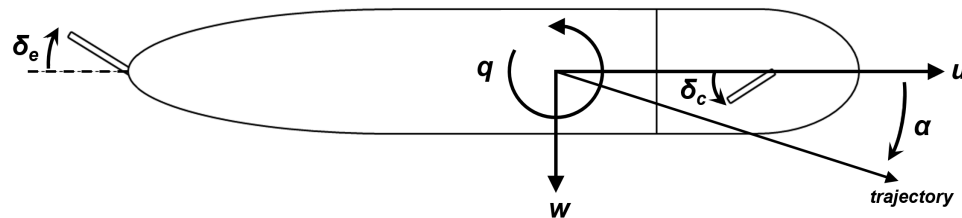


Figure 2.3 – STARBOARD-SIDE VIEW OF A GENERIC AUV BODY.

3. FIN ANGLE SIGN CONVENTION

For an individual control surface, the positive axis of rotation points away from the vehicle body. Positive rotation of the control surface is defined to be consistent with the positive direction of the axis of rotation, and can be identified by using the conventional right-hand rule, as indicated in Figure 3.1.

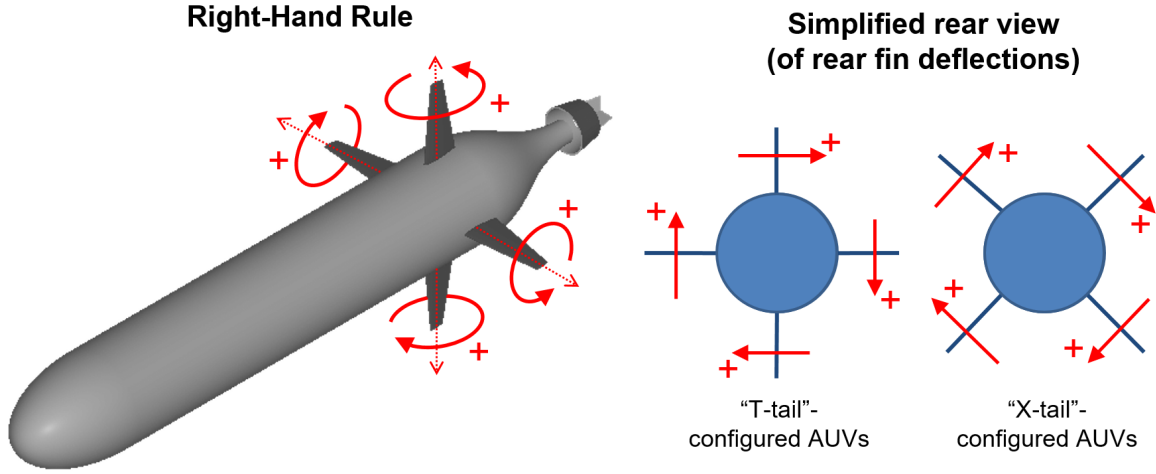


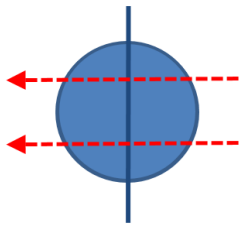
Figure 3.1 – SIGN CONVENTION FOR CONTROL SURFACE ANGULAR DEFLECTIONS.

3.1 Implementation of Traditional Rudder Commands onto Rear Fins

For any control-command, all rear fins are deflected by the same amount δ given by the command, in the appropriate direction for the task. Figure 3.2 shows the simplified rear views (of rear fin deflections) during different control-commands on an X-tailed craft, detailing the implementation from controller commands to fin rotation.

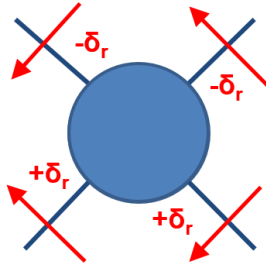
Command: desired rudder = δ_r (radians)

Virtual Single Rudder Fin



Imaginary rudder fin deflects exactly δ_r -radians to the left.

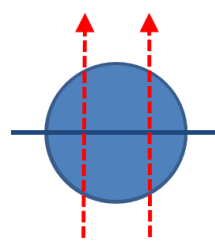
Actual Implementation



All fins deflect by an extra δ_r -radians to the left.

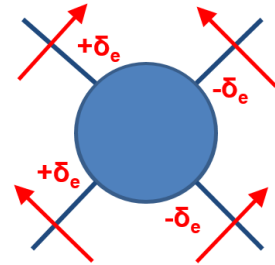
Command: desired elevator = δ_e (radians)

Virtual Single Elevator Fin



Imaginary elevator fin deflects exactly δ_e -radians upward.

Actual Implementation



All fins deflect by an extra δ_e -radians upward.

Figure 3.2 – IMPLEMENTATION OF δ_R AND δ_E ONTO REAR FINS IN AN X-TAILED UUV.

This trivial methodology for control surface actuation is used for the X and T-tail AUV configurations presented in this study. For generic n-finned AUVs, a universal approach is presented later in Section 3.6.

3.2 Basic Rudder Command Roll Compensation (as Opposed to Roll Control)

We present a scenario where the trajectory needs to turn leftward and upward, but the craft has rolled by a nonzero angle ϕ . For any command combination $(\delta_{r,desired}, \delta_{e,desired})$, the roll must be compensated for in the body-frame to maneuver properly in the world-frame, as illustrated in Figure 3.3. Any “desired” turning command directions are in the world frame, while “actual” final turning commands are effectuated in the body frame of the craft.

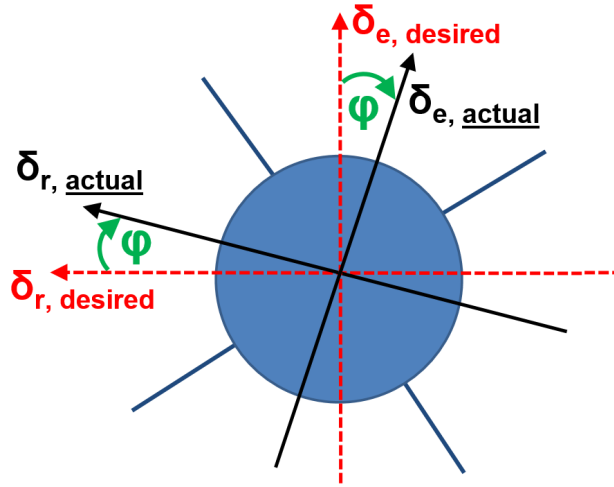


Figure 3.3 – SIMPLIFIED REAR VIEW OF ROLL COMPENSATION IN TURNING.

The final commands (δ_r , δ_e , δ_c) interpreted by the craft for control surface actuation are then

$$\begin{aligned}\delta_r &= \delta_{r, \text{actual}} = \delta_{r, \text{desired}} \cos \phi - \delta_{e, \text{desired}} \sin \phi \\ \delta_e &= \delta_{e, \text{actual}} = \delta_{r, \text{desired}} \sin \phi + \delta_{e, \text{desired}} \cos \phi \\ \delta_c &= \delta_{c, \text{actual}} = \delta_{c, \text{desired}} \cos \phi\end{aligned}\tag{3.1}$$

3.3 Roll Control

We can command roll by adding a new control parameter δ_{roll} . Unlike δ_r and δ_e , δ_{roll} is independent of current roll orientation ($\delta_{\text{roll}} = \delta_{\text{roll}, \text{desired}} = \delta_{\text{roll}, \text{actual}}$, always). Roll parameter δ_{roll} is manifested by deflecting all rear fins an extra δ_{roll} radians clockwise. A new hydrodynamic coefficient $K_{uu\delta_{\text{roll}}}$ is developed to describe the roll-moment on the craft due to roll-command δ_{roll} . $K_{uu\delta_{\text{roll}}}$ is always defined as negative. The implementation of δ_{roll} onto control surfaces is shown in Figure 3.4.

Command: desired roll = δ_{roll} (radians)

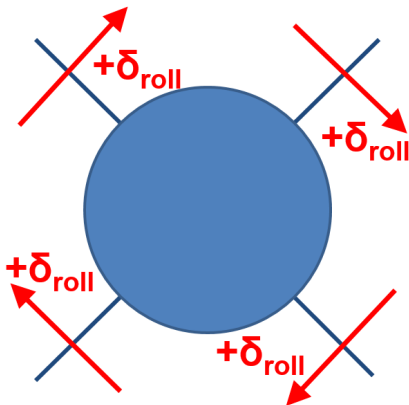


Figure 3.4 – IMPLEMENTATION OF ROLL CONTROL PARAMETER δ_{ROLL} ON REAR CONTROL SURFACES.

3.4 Control-Command Superposition on Rear Fins

Lateral forces and hull-moments from the rear fins scale linearly with fin deflection angle. Likewise, the net elevator force resulting from δ_e does not interfere with the net rudder force resulting from δ_r . The addition of constant offset δ_{roll} also does not interfere the total control surface forces resulting from δ_r and δ_e . Therefore, the fin deflections from δ_r , δ_e , and δ_{roll} can be superimposed to achieve yaw, pitch, and roll control simultaneously, as shown in Figure 3.5:

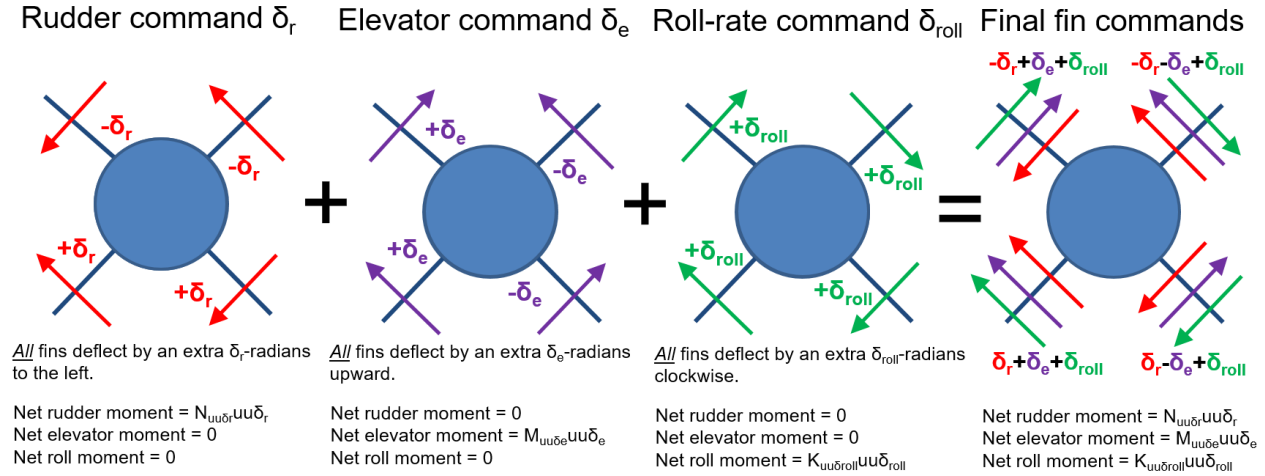


Figure 3.5 – IMPLEMENTATION OF SIMULTANEOUS δ_R , δ_E , AND δ_{ROLL} COMMANDS VIA SUPERPOSITION.

A superposition example is presented where the roll parameter is ignored for explanation purposes. If $\delta_r = \delta_e = 10$ degrees, we observe how pitch and yaw commands superimpose in Figure 3.6:

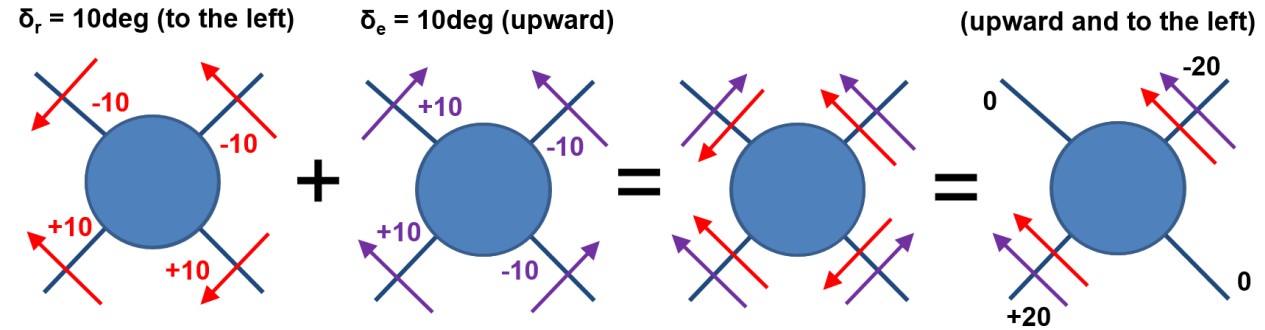


Figure 3.6 – CONCEPTUAL EXAMPLE OF SIMULTANEOUS MANEUVERS $\delta_R = \delta_E = 10$ DEGREES.

Any fin angles exceeding the maximum allowable physical deflection saturate at the maximum allowable angle. Figure 3.7 presents pseudo-code that implements and saturates the final fin angles from control-commands on a four-fin X-tail configuration.

% Initially superimpose angle commands accordingly

```

% If X-tail Configuration
Top_Portside_Fin_Angle = -δr + δe + δroll
Top_Starboard_Fin_Angle = -δr - δe + δroll
Bottom_Portside_Fin_Angle = δr + δe + δroll
Bottom_Starboard_Fin_Angle = δr - δe + δroll

% If T-tail Configuration
Top_Fin_Angle = -δr + δroll
Bottom_Fin_Angle = δr + δroll
Portside_Fin_Angle = δe + δroll
Starboard_Fin_Angle = -δe + δroll

% Then clip any angles surpassing an allowed limit
if abs(fin_angle) >= (maximum_allowed_angle)
    fin_angle = sign(fin_angle)*maximum_allowed_angle
end

```

Figure 3.7 – PSEUDO-CODE IMPLEMENTATION OF δ_R , δ_E , AND δ_{ROLL} COMMANDS ONTO CONTROL SURFACES.

3.5 Reconstructing δ_r , δ_e , and δ_{roll} from Clipped Fin Angles for Control Force Estimation

Since all rudder forces (except along \hat{x} in the body-frame) vary linearly with rudder angle, commands δ_r , δ_e , and δ_{roll} can be reconstructed from the clipped fin angles straightforwardly, as shown for an X-tail configuration in Figure 3.8. This would be done for simulation and modelling purposes, because control forces and moments on the hull are calculated from δ -commands, which are warped through actuator clipping. These reconstructed unclipped-equivalent δ -commands yield the clipped fin angles upon implementation.

```

δr = mean([-Top_Portside_Fin_Angle, -Top_Starboard_Fin_Angle, Bottom_Portside_Fin_Angle, Bottom_Starboard_Fin_Angle]);
δe = mean([Top_Portside_Fin_Angle, -Top_Starboard_Fin_Angle, Bottom_Portside_Fin_Angle, -Bottom_Starboard_Fin_Angle]);
δroll = mean([Top_Portside_Fin_Angle, Top_Starboard_Fin_Angle, Bottom_Portside_Fin_Angle, Bottom_Starboard_Fin_Angle]);

```

Figure 3.8 – PSEUDO-CODE OF THE EXTRACTION OF δ_R , δ_E , AND δ_{ROLL} COMMANDS FROM CLIPPED CONTROL-SURFACE ANGLES ON AN X-TAILED UUV.

Likewise, pseudo-code for extracting δ -commands from clipped fin angles for a T-tailed UUV is shown in Figure 3.9:

```

δr = mean([-Top_Fin_Angle, Bottom_Fin_Angle]);
δe = mean([Portside_Fin_Angle, -Starboard_Fin_Angle]);
δroll = mean([Top_Fin_Angle, Bottom_Fin_Angle, Portside_Fin_Angle, Starboard_Fin_Angle]);

```

Figure 3.9 – PSEUDO-CODE OF THE EXTRACTION OF δ_R , δ_E , AND δ_{ROLL} COMMANDS FROM CLIPPED CONTROL-SURFACE ANGLES ON A T-TAILED UUV.

Then lastly, we calculate the new X-forces by summing together the drag forces from each individual rear fin, as the X-force from each fin scales with the square the deflection angle. Assuming there are n rear-fins total, the force along \hat{x} from any individual fin i with net angular deflection δ_i is

$$X_i = \frac{1}{n} X_{uu\delta\delta} u^2 \delta_i^2 \quad (3.2)$$

When applying Figure 3.7 (or Equation 3.5) into δ_i , the control surface force along \hat{x} due to all rear fin deflections can be defined in terms of the newly-reconstructed δ -commands after clipping:

$$X_{RearFins} = \frac{1}{n} X_{uu\delta\delta} u^2 \sum_{i=1}^n \delta_i^2 = X_{uu\delta\delta} u^2 (\delta_r^2 + \delta_e^2 + \delta_{roll}^2) \quad (3.3)$$

where δ_r , δ_e , and δ_{roll} are the reconstructed commands from clipped fin angles δ_i . The total control surface force along \hat{x} due to all deflections on fins and canards is then

$$X_{ControlSurfaces} = X_{uu\delta\delta} u^2 (\delta_r^2 + \delta_e^2 + \delta_{roll}^2) + X_{uu\delta c} u^2 \delta_c^2 \quad (3.4)$$

3.6 Generic Approach to Control-Command Implementation

A universal approach can be used to implement rudder commands onto rear fins in any arrangement. This generic methodology still applies if the number of tail fins n is odd or greater than 4, and is identical to our current T-tail control implementation. It would also work in replacement for our current X-tail control strategy. Parameters for the generalized approach for rudder-command implementation onto rear fins are outlined in Figure 3.10.

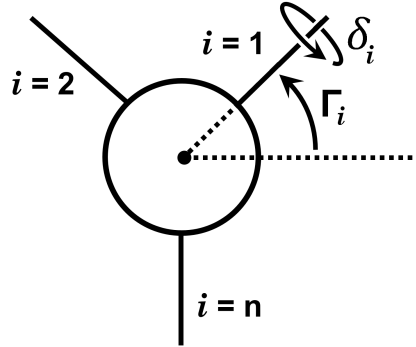


Figure 3.10 – SIMPLIFIED REAR VIEW AND SIGN CONVENTION OF A GENERIC N-FINNNED AUV.

Before fin angle limits are considered, the angular deflection δ_i of any tail fin i is actuated as

$$\delta_i = -\delta_r \sin(\Gamma_i) - \delta_e \cos(\Gamma_i) + \delta_{roll} \quad (3.5)$$

After fin angle saturation and clipping, control commands δ_r , δ_e , and δ_{roll} can be reconstructed from *relevant* clipped control-surface angles δ on any AUV tail configuration using the generalized approach.

$$\delta_r = -\frac{1}{n_r} \sum_{i=1}^n \delta_i \csc(\Gamma_i), \Gamma_i \notin \{0, \pi\} \quad (3.6)$$

$$\delta_e = -\frac{1}{n_e} \sum_{i=1}^n \delta_i \sec(\Gamma_i), \Gamma_i \notin \{\frac{\pi}{2}, \frac{3\pi}{2}\} \quad (3.7)$$

$$\delta_{roll} = \frac{1}{n} \sum_{i=1}^n \delta_i \quad (3.8)$$

where n_r is the number of rear fins that are not positioned at $\Gamma_i = 0$ or $\Gamma_i = \pi$, and n_e is the number of rear fins that are not positioned at $\Gamma_i = \frac{\pi}{2}$ or $\Gamma_i = \frac{3\pi}{2}$.

It is important to note that for X-tail configurations, the realization of δ_r and δ_e onto fins could be defined using either of the two methods presented. Some studies assume this generic rudder-command implementation for X-tail control, while others instead utilize the traditional approach (Section 3.1) used throughout this study. The conversion between the two X-tail control methods is trivial (generalized $\delta_r = \sqrt{2}$ (traditional δ_r)) but must be considered whenever comparing two different X-tail models.

4. KINEMATICS

Referring back to Figure 2.1, the position of the AUV is now described with $\eta = [\eta_1^\top, \eta_2^\top]^\top$ where $\eta_1 = [x, y, z]$ is the location of the center of buoyancy of the AUV in an world reference frame and $\eta_2 = [\phi, \theta, \psi]$ is the set of Euler angles roll, pitch, and yaw that define orientation of the AUV relative to the world reference frame. The world-frame position vector η is then

$$\eta = [x, y, z, \phi, \theta, \psi]^\top \quad (4.1)$$

The velocity of the AUV is $\nu = [\nu_1^\top, \nu_2^\top]^\top$ where $\nu_1 = [u, v, w]$ is the set of body-relative velocities surge, sway, and heave, and $\nu_2 = [p, q, r]$ is the set of right-handed angular velocities about the positive X , Y , and Z axes of the body reference frame. The body-frame motion state vector ν is then

$$\nu = [u, v, w, p, q, r]^\top \quad (4.2)$$

In modeling and simulation, world-frame position vector η is integrated from $\dot{\eta}$. The derivative $\dot{\eta}$ is calculated and updated from the current body-frame motion-states vector ν and the last known orientation-components of η from the previous timestep (ϕ, θ, ψ):

$$J_1 := \begin{bmatrix} \cos(\psi) \cos(\theta) & \cos(\psi) \sin(\varphi) \sin(\theta) - \cos(\varphi) \sin(\psi) & \sin(\varphi) \sin(\psi) + \cos(\varphi) \cos(\psi) \sin(\theta) \\ \cos(\theta) \sin(\psi) & \cos(\varphi) \cos(\psi) + \sin(\varphi) \sin(\psi) \sin(\theta) & \cos(\varphi) \sin(\psi) \sin(\theta) - \cos(\psi) \sin(\varphi) \\ -\sin(\theta) & \cos(\theta) \sin(\varphi) & \cos(\varphi) \cos(\theta) \end{bmatrix}$$

$$J_2 := \begin{bmatrix} 1 & \sin(\varphi) \tan(\theta) & \cos(\varphi) \tan(\theta) \\ 0 & \cos(\varphi) & -\sin(\varphi) \\ 0 & \frac{\sin(\varphi)}{\cos(\theta)} & \frac{\cos(\varphi)}{\cos(\theta)} \end{bmatrix}$$

$$\dot{\eta} = \begin{bmatrix} J_1 & [0] \\ [0] & J_2 \end{bmatrix} \nu \quad (4.3)$$

5. DYNAMICS

The six-degree of freedom (DOF) dynamic equations, following Newtonian mechanics, for a vehicle maneuvering in deeply submerged conditions [7], are as follows:

$$\underbrace{(M_{RB} - M_A)\dot{\nu}}_{\text{Mass + Added Mass}} + \underbrace{(C_{RB}(\nu) - C_A(\nu))\nu}_{\text{Coriolis + Added Coriolis}} + \underbrace{D(\nu)\nu}_{\text{Friction + Damping}} + \underbrace{G(\eta)}_{\text{Gravitational Forces}} = \underbrace{\tau}_{\text{Control Forces}} \quad (5.1)$$

where the $M_{RB}\dot{\nu} + C_{RB}(\nu)\nu$ represents rigid-body dynamics. The terms $M_A\dot{\nu} + C_A(\nu)\nu$ are due to added mass, $D(\nu)\nu$ refers to hydrodynamic damping, $G(\eta)$ accounts for gravity and buoyancy, and $\tau \in \mathbb{R}^{6 \times 1}$ refers to control surfaces and propulsion.

The external hydrodynamic forces due to the hull motion in the fluid are explicitly isolated on the left hand side and expressed by the added mass M_A and damping terms C_A, D . These terms follow a common conceptual idealization of hydrodynamic (reaction) forces originated as a consequence of the body accelerated motion when deeply submerged into a fluid. They follow the simplifying assumption that hydrodynamic forces can be expressed as a linear combination of components proportional to the body acceleration and to the square of the velocity.

In the following section, we will particularize the elements of each matrix, retaining only the most important terms, selected and defined with specific reference to the method used to determine their value. In particular, we use a set of virtual, CFD based, forced motion experiments to infer their value, instead of the approximate semi-empirical methods (as for instance used by [17]) that are commonly used in early design stage. These methods are typically based on potential flow assumption, strip methods to reduce the 3D problem on simpler 2D flow problem on cross sections of the body and add viscous forces as a correction to potential flow forces. All these assumption fail in the case of complicated (realistic) hull shapes subject to large angles of attack of the inflow.

A system identification approach is used in our case to determine the value of the damping and added mass terms, applied to an appropriate set of forced motion maneuvers specifically defined to facilitate the identification of the individual coefficients. Non-linear effects can be characterized by extending the set of prescribed maneuvers to consider same motion with different amplitudes or frequencies.

5.1 Mass and Payload Distribution

Our AUVs are designed to be on the order of 0.2% buoyant. Any encapsulated water in the craft (inside pockets, etc.) is considered to be part of the hull dynamically, so enclosed water is treated as part of rigid-body mass and moment of inertia. In this sense, dynamic ballasts alter the effective overall mass of the AUV, but do not change the buoyant displacement. The center of buoyancy should be above the center of gravity for proper orientation-restoring forces, and the $[0,0,0]$ point is located at the center of buoyancy, not gravity, of the craft. By this convention, dynamic ballasts alter the position of the center of *gravity* of the vehicle. Making the separation distance between buoyancy and gravity centers too large primarily hinders maximum pitch capability, while minimally affecting yaw-axis performance.

5.2 Rigid-body Dynamics

From [6], the mass matrix M_{RB} in (5.1) is expressed

$$M_{RB} = \begin{bmatrix} m & 0 & 0 & 0 & mz_G & -my_G \\ 0 & m & 0 & -mz_G & 0 & mx_G \\ 0 & 0 & m & my_G & -mx_G & 0 \\ 0 & -mz_G & my_G & I_x & -I_{xy} & -I_{xz} \\ mz_G & 0 & -mx_G & -I_{yx} & I_y & -I_{yz} \\ -my_G & mx_G & 0 & -I_{zx} & -I_{zy} & I_z \end{bmatrix} \quad (5.2)$$

where m is the mass of the AUV and $C_G = [x_G, y_G, z_G]^T$ is the center of mass of the vehicle with respect to the center of buoyancy. The moment of inertia components I_{ij} are computed directly using CAD software and vehicle geometries. If unavailable, the moments of inertia for a cylinder can instead be used to roughly approximate the moments of inertia of the vehicle body [1], from which $I_x = \frac{1}{2}mr^2$, and $I_y = I_z = \frac{1}{12}m(3r^2 + L^2)$ where r is the radius of the cylinder, L is the length, and off-axis terms $I_{ij, i \neq j}$ are ignored.

The matrix $C_{RB}(\nu)$ appearing in (5.1), that includes rigid body Coriolis and centrifugal forces, is expanded here:

$$C_{RB}(\nu) = \begin{bmatrix} 0 & 0 & 0 & m(y_G q + z_G r) & -m(x_G q - w) & -m(x_G r + v) \\ 0 & 0 & 0 & -m(y_G p + w) & m(z_G r + x_G p) & -m(y_G r - u) \\ 0 & 0 & 0 & -m(z_G p - v) & -m(z_G q + u) & m(x_G p + y_G q) \\ -m(y_G q + z_G r) & m(y_G q) & m(z_G p) & 0 & -I_{yz} q - I_{xz} p + I_z r & I_{yz} r + I_{xy} p - I_y q \\ m(x_G q) & -m(z_G r + x_G p) & m(z_G q) & -I_{yz} q + I_{xz} p - I_z r & 0 & -I_{xz} r - I_{xy} q + I_x p \\ m(x_G r) & m(y_G r) & -m(x_G p + y_G q) & -I_{yz} r - I_{xy} p + I_y q & I_{xz} r - I_{xy} q - I_x p & 0 \end{bmatrix} \quad (5.3)$$

5.3 Added Inertia Dynamics

Under the assumption of approximate port/starboard symmetry and loose top/bottom symmetry, the only non-zero or non-negligible coefficients used for added inertia are

$$\{X_{\dot{u}}, Y_{\dot{v}}, Z_{\dot{w}}, K_{\dot{p}}, M_{\dot{q}}, N_{\dot{r}}, Y_{\dot{r}}, Z_{\dot{q}}\} \quad (5.4)$$

The added inertia matrix M_A in (5.1) is then

$$M_A = \begin{bmatrix} X_{\dot{u}} & 0 & 0 & 0 & 0 & 0 \\ 0 & Y_{\dot{v}} & 0 & 0 & 0 & Y_{\dot{r}} \\ 0 & 0 & Z_{\dot{w}} & 0 & Z_{\dot{q}} & 0 \\ 0 & 0 & 0 & K_{\dot{p}} & 0 & 0 \\ 0 & 0 & M_{\dot{w}} & 0 & M_{\dot{q}} & 0 \\ 0 & N_{\dot{v}} & 0 & 0 & 0 & N_{\dot{r}} \end{bmatrix} \quad (5.5)$$

From the way many of the coefficients are estimated, the star-coefficients in $D(\nu)$ that are derived via VPMM (see Section 6) already account for many of the commonly referenced terms in the added-Coriolis matrix C_A . For example, the term N_{ur}^* already accounts for all components multiplying $u \cdot r$ into N . Under the same loose symmetry assumptions used in M_A , while also avoiding force redundancies from $D(\nu)$, the added Coriolis matrix $C_A(\nu)$ in (5.1) is

$$C_A(\nu) = \begin{bmatrix} 0 & 0 & 0 & 0 & 0 & 0 \\ 0 & 0 & 0 & Z_{\dot{w}} w + Z_{\dot{q}} q & 0 & 0 \\ 0 & 0 & 0 & -Y_{\dot{v}} v - Y_{\dot{r}} r & 0 & 0 \\ 0 & -Z_{\dot{w}} w - Z_{\dot{q}} q & Y_{\dot{v}} v + Y_{\dot{r}} r & 0 & -N_{\dot{v}} v - N_{\dot{r}} r & M_{\dot{w}} w + M_{\dot{q}} q \\ 0 & 0 & 0 & N_{\dot{v}} v + N_{\dot{r}} r & 0 & -K_{\dot{p}} p \\ 0 & 0 & 0 & -M_{\dot{w}} w - M_{\dot{q}} q & K_{\dot{p}} p & 0 \end{bmatrix} \quad (5.6)$$

5.4 Hydrodynamic damping

Forces τ_D due to hydrodynamic damping in (5.1) are expressed $\tau_D = D(\nu)\nu$ where due to the assumptions of approximate top/bottom symmetry and loose port/starboard symmetry, the matrix of coefficients can be simplified to

$$D(\nu) = - \begin{bmatrix} X_{uu}|u| & 0 & 0 & 0 & 0 & 0 \\ 0 & Y_{vv}|v| + Y_{uv}u & 0 & 0 & 0 & Y_{rr}|r| + Y_{ur}^*u \\ 0 & 0 & Z_{ww}|w| + Z_{uw}u & 0 & Z_{qq}|q| + Z_{uq}^*u & 0 \\ 0 & 0 & 0 & K_{pp}|p| + K_{up}u & 0 & 0 \\ 0 & 0 & M_{ww}|w| + M_{uw}^*u & 0 & M_{qq}|q| + M_{uq}^*u & 0 \\ 0 & N_{vv}|v| + N_{uv}^*u & 0 & 0 & 0 & N_{rr}|r| + N_{ur}^*u \end{bmatrix} \quad (5.7)$$

5.5 Gravitational Restoring Forces and Moments

The effects of gravity and buoyancy are modelled

$$G(\eta) = 9.81 \cdot \begin{bmatrix} (m - b) \sin(\theta) \\ -(m - b) \cos(\theta) \sin(\phi) \\ -(m - b) \cos(\theta) \cos(\phi) \\ -y_G m \cos(\theta) \cos(\phi) + z_G m \cos(\theta) \sin(\phi) \\ z_G m \sin(\theta) + x_G m \cos(\theta) \cos(\phi) \\ -x_G m \cos(\theta) \sin(\phi) - y_G m \sin(\theta) \end{bmatrix} \quad (5.8)$$

where m is the effective mass of the submerged body with possible dynamic ballasting, b is the buoyant displacement, $[x_G, y_G, z_G]^\top$ is the location of the center of gravity in the body frame after ballasting, with buoyancy center $[x_B, y_B, z_B]^\top := [0, 0, 0]$ by definition.

5.6 Control Forces and Moments

For control surfaces in a any configuration, the effect of control surfaces and of the propulsor are modelled as

$$\tau = \begin{bmatrix} (\text{Thrust}) + X_{uu\delta\delta} u^2 (\delta_r^2 + \delta_e^2 + \delta_{\text{roll}}^2) + X_{uu\delta\delta_c} u^2 \delta_c^2 \\ Y_{uu\delta_r} u^2 \delta_r \\ Z_{uu\delta_e} u^2 \delta_e + Z_{uu\delta_c} u^2 \delta_c \\ K_{uu\delta_{\text{roll}}} u^2 \delta_{\text{roll}} \\ M_{uu\delta_e} u^2 \delta_e + M_{uu\delta_c} u^2 \delta_c \\ N_{uu\delta_r} u^2 \delta_r \end{bmatrix} \quad (5.9)$$

where the virtual control surfaces δ_r , δ_e , and δ_{roll} have been reconstructed from physical fin deflections in accordance with Sections 3.5 - 3.6. Virtual control surface δ_c is the canard angle deflection command sent to all canards, described in Section 2.

5.7 Final Update Laws

The final update laws used in dynamic modeling are then constructed from Equations (4.3) and (5.1):

$$\begin{aligned} \dot{\nu} &= [M_{RB} - M_A]^{-1} [(C_A(\nu) - C_{RB}(\nu))\nu - D(\nu)\nu - G(\eta) + \tau] \\ \dot{\eta} &= \begin{bmatrix} J_1(\eta) & [0] \\ [0] & J_2(\eta) \end{bmatrix} \nu \end{aligned} \quad (5.10)$$

where $J_1(\eta)$ and $J_2(\eta)$ are defined in Equation (4.3).

6. HYDRODYNAMIC COEFFICIENTS ESTIMATION

Hydrodynamic 6-DOF hull coefficient estimation is based primarily on virtual maneuvers performed in the isolated horizontal plane (yaw axis). Although some of the pitch-axis coefficients are symmetric with their yaw-axis counterparts, pitch axis hull coefficients are estimated by performing the same yaw-axis maneuvers with the craft rotated 90° in roll. The process for estimating horizontal plane coefficient estimation will be detailed thoroughly, followed by a straightforward method to repeat the process for pitch-axis coefficient estimation. In restricting our attention to maneuvers in the horizontal plane, only three differential equations are relevant for the three degrees of freedom in that plane: surge, sway and yaw. Relevant dynamic motion states are shown in Fig. 6.1.

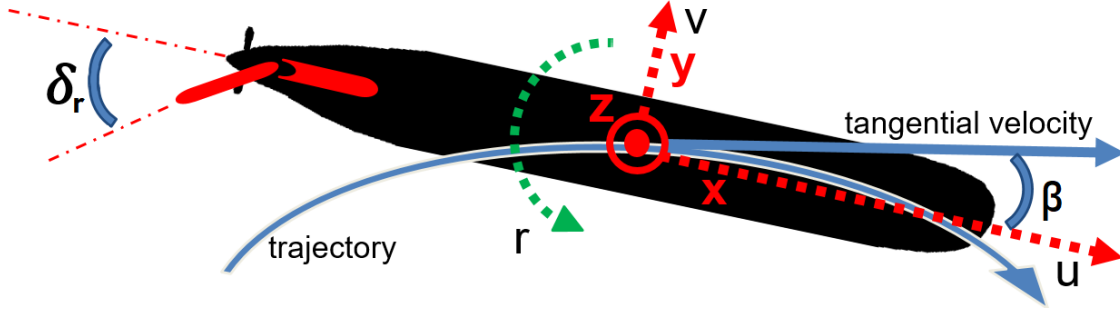


Figure 6.1 – OVERVIEW OF RELEVANT PLANAR-MOTION PARAMETERS.

Surge velocity u is defined along x body axis direction, sway velocity v is along y , and yaw rotation rate r is about z . The body reference frame center is the vehicle center of buoyancy. Dynamic ballasting acts on the center of gravity.

When the system of dynamic equations (4.3) in 6-DOF is confined to the horizontal plane motion, ignoring the effect of roll, the complete system is represented by the following system of lumped-parameter differential equations:

$$(\dot{u} - vr - x_G r^2)m = X_{ext} + X_{\dot{u}}\dot{u} + X_{uu}u|u| + X_{uu\delta_r}u|\delta_r|^2 \quad (6.1)$$

$$\begin{aligned} (\dot{v} + ur)m &= Y_{ext} + Y_{uv}uv + Y_{vv}v|v| + Y_{\dot{v}}\dot{v} + Y_{ur}^*ur \\ &\quad + Y_{rr}r|r| + Y_{\dot{r}}\dot{r} + Y_{uu\delta_r}u|\delta_r| \end{aligned} \quad (6.2)$$

$$\begin{aligned} \dot{r}I_{zz} + (\dot{v} + ru)m x_G &= N_{ext} + N_{uv}^*uv + N_{vv}v|v| + N_{\dot{v}}\dot{v} + N_{ur}^*ur \\ &\quad + N_{rr}r|r| + N_{\dot{r}}\dot{r} + N_{uu\delta_r}u|\delta_r| \end{aligned} \quad (6.3)$$

where x_G is the x -coordinate of the center of gravity, and in this case the only additional external force is X_{ext} equal to the thrust delivered by the propeller, approximated to a constant magnitude equal to the drag at the design speed u_0 , i.e. $X_{ext} = -X_{uu}u_0^2$. The rectilinear uniform motion with speed u_0 is taken as reference steady state equilibrium condition for the expansion of hydrodynamic forces that leads to the definition of the hydrodynamic derivatives. Coefficient Y_{ur}^* is the summation of all elements multiplying $u \cdot r$ into Y , accounting for both added-Coriolis and viscous damping effects. The sub-components of Y_{ur}^* are uncoupled from one-another in estimation and maneuvering-model implementation, allowing for such parameter grouping. Likewise, coefficients N_{ur}^* and N_{uv}^* comprise of all elements multiplying $u \cdot r$ and $u \cdot v$ into N , respectively.

6.1 Estimation of Hull Coefficients

Hull coefficients are estimated using virtual planar mechanism simulations, which are first-order unsteady CFD simulations [10] that replicate the maneuvers performed in captive tests on ship models in towing tanks using planar motion mechanisms (PMMs). *Virtual PMM (VPMM)* tests are conducted using time-resolved viscous flow K-Epsilon solvers, with the ability to consider for moving meshes, by prescribing body motions and calculating hydrodynamic pressure and shear force and moments on the moving body. Because the motion is prescribed, dry mass m and rotary inertia I_{zz} are not relevant for these tests.

6.1.1 Pure-Sway

Estimation of coefficients Y_{uv} , Y_{vv} , $Y_{\dot{v}}$, N_{uv}^* , N_{vv} , and $N_{\dot{v}}$ is based on measurement of lateral force Y and moment N in the captive *pure-sway* VPMM test, where the AUV hull (with appendages) is prescribed a constant surge velocity u and a pure sinusoidal sway motion with velocity $v(t)$. Yaw rotation rate r is fixed to zero. The magnitude of the sway oscillation amplitude is chosen to be on the order of a few percent of the AUV length, and the frequency is chosen to be 0.667Hz [3, 16]. The PMM frequency was chosen based in part on the results from a study performed in 2007 [16] that analyzed different VPMM oscillation frequencies for a craft of similar length and design speed. This oscillation frequency is low enough to circumvent frequency-dependence and is used in all VPMM tests. A timestep of 1ms guarantees sufficient samples per oscillation period. A snapshot of a pure-sway VPMM test is presented in Fig. 6.2.

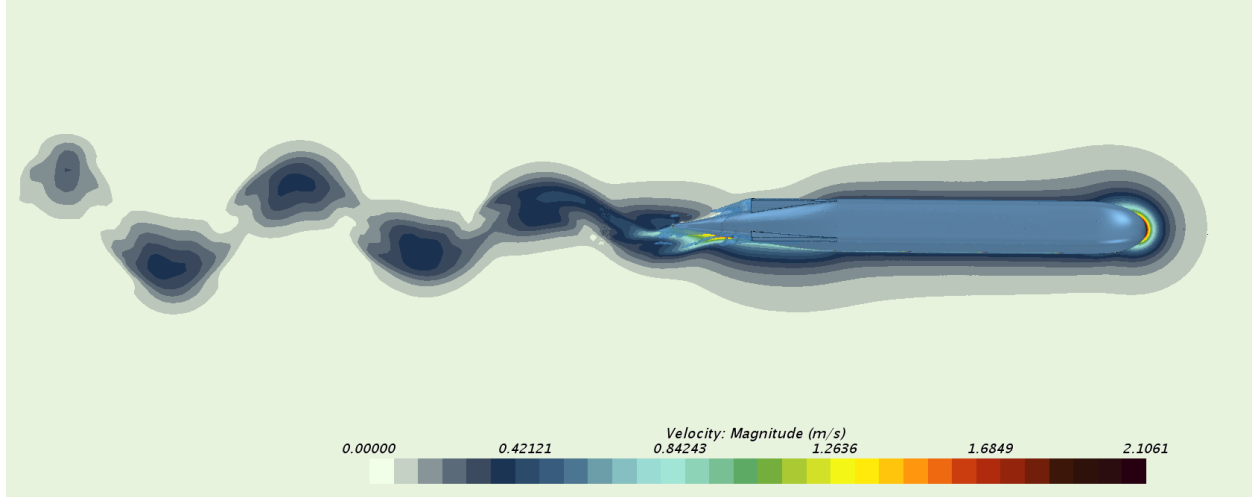


Figure 6.2 – INDUCED VELOCITY FIELD (HORIZONTAL PLANE) IN THE FLUID EXCITED BY THE VEHICLE UNDERGOING A 10CM-AMPLITUDE PURE-SWAY VPMM TEST.

For captive pure-sway VPMM tests, AUV dynamics (Eqs. 6.1-6.3) simplify to

$$Y_{\text{meas}}(t) = Y_{uv}u(t)v(t) + Y_{vv}v(t)|v(t)| + Y_{\dot{v}}(t)\dot{v}(t) \quad (6.4)$$

$$N_{\text{meas}}(t) = N_{uv}^*u(t)v(t) + N_{vv}v(t)|v(t)| + N_{\dot{v}}(t)\dot{v}(t) \quad (6.5)$$

where $Y_{\text{meas}}(t)$ is the unsteady hydrodynamic force component measured in the sway direction and $N_{\text{meas}}(t)$ is the unsteady moment induced by the hydrodynamic force in the yaw direction. In the sequel, explicit dependence on t is suppressed in our notation where doing so does not diminish clarity.

Pure sway VPMM tests are conducted for three separate sway amplitudes for better recursion during coefficient estimation. Figure 6.3 shows the concatenated output.

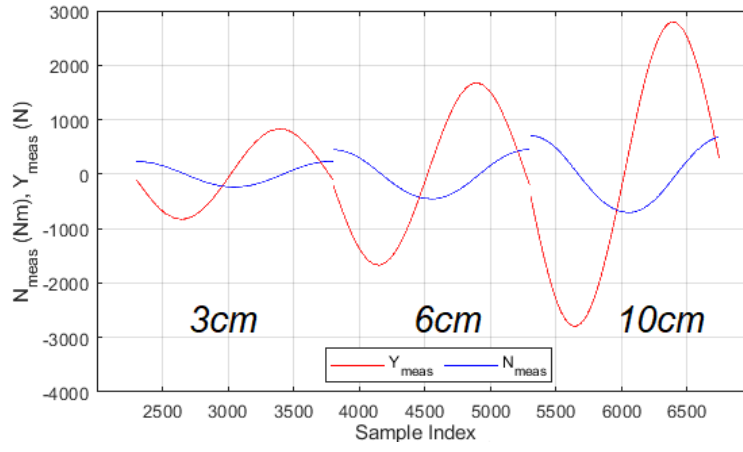


Figure 6.3 – PURE-SWAY VPMM TESTS WITH THREE AMPLITUDES (INDICATED IN CM ON THE GRAPH): CALCULATED SIDE FORCE AND YAW MOMENT.

Data vectors corresponding to the time history of Y_{meas} , N_{meas} , uv , $v|v|$, and \dot{v} are created by sampling each signal n times for each amplitude. The data vectors are then arranged with their three amplitude series concatenated one after another, in order to form 5 individual column vectors each with $3n$ elements \vec{Y}_{meas} , \vec{N}_{meas} , \vec{uv} , $\vec{v|v|}$, $\vec{\dot{v}}$, each in \mathbb{R}^{3n} . A new matrix V is created arranging the motion-state vectors one beside the other. Specifically, $V = [\vec{uv}, \vec{v|v|}, \vec{\dot{v}}] \in \mathbb{R}^{3n \times 3}$. The hydrodynamic coefficients are estimated

$$[Y_{uv} \ Y_{vv} \ Y_{\dot{v}}]^T = V^\dagger \vec{Y}_{\text{meas}} \quad (6.6)$$

$$[N_{uv}^* \ N_{vv} \ N_{\dot{v}}]^T = V^\dagger \vec{N}_{\text{meas}} \quad (6.7)$$

where $V^\dagger := (V^T V)^{-1} V^T$ is the pseudo-inverse of non-square matrix V .

The coefficients can be used to reconstruct Y and N to visualize the accuracy of the reduced-order AUV dynamics. In Fig. 6.4, measured forces and moments are compared with their coefficient-reconstructed counterparts.

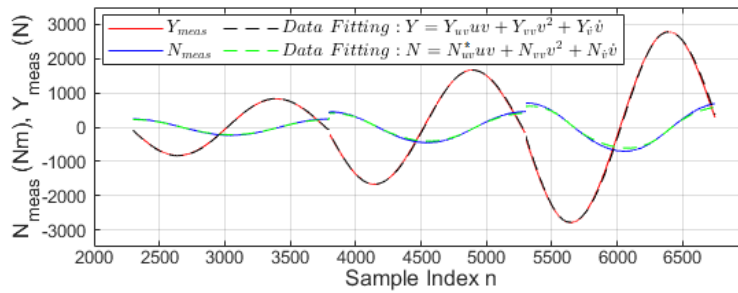


Figure 6.4 – PURE-SWAY VPMM TESTS WITH THREE AMPLITUDES.

6.1.2 Pure-Yaw

The hydrodynamic parameters that are dependent on the yaw rate, Y_{ur}^* , Y_{rr} , $Y_{\dot{r}}$, N_{ur}^* , N_{rr} , and $N_{\dot{r}}$, are identified from the *pure-yaw* VPMM test. This maneuver uses the same constant surge velocity with the same sinusoidal body-frame origin trajectory as the pure-surge maneuver, but a sinusoidal rotational speed is also prescribed such that the sway velocity v (measured in the body-frame) is always zero. Equivalently, the x -axis of the body-frame (see Fig. 6.1) remains tangent to the trajectory of the body-frame origin at all times. A snapshot of the pure-yaw VPMM test is presented in Fig. 6.5:

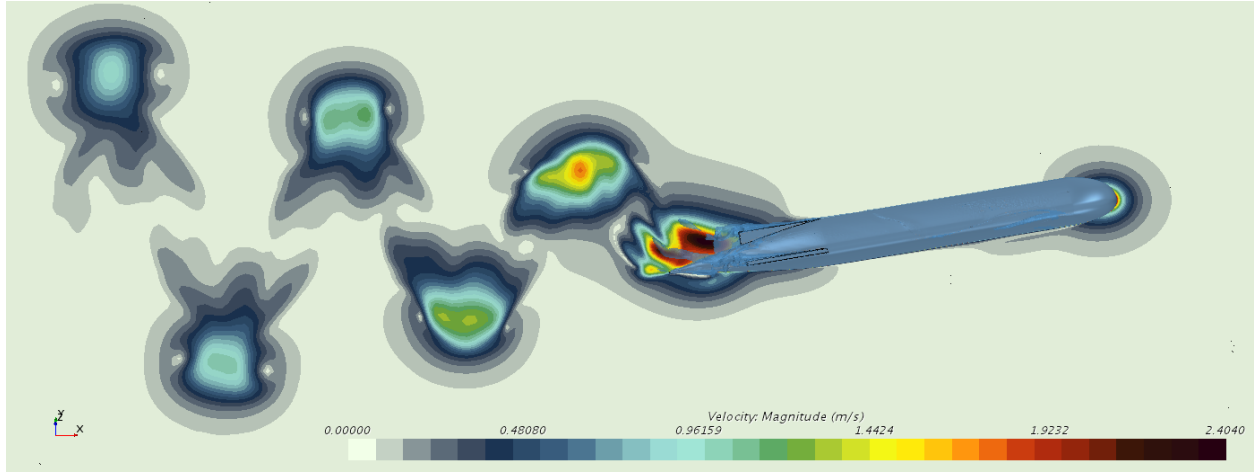


Figure 6.5 – INDUCED VELOCITY FIELD (HORIZONTAL SYMMETRY PLANE) IN THE FLUID EXCITED BY THE VEHICLE UNDERGOING THE 10CM-AMPLITUDE PURE-YAW VPMM TEST.

For the pure-yaw VPMM trial, AUV dynamics (Eqs. 6.1-6.3) simplify to

$$Y_{\text{meas}} = Y_{ur}^* ur + Y_{rr} r|r| + Y_{\dot{r}} \dot{r} \quad (6.8)$$

$$N_{\text{meas}} = N_{ur}^* ur + N_{rr} r|r| + N_{\dot{r}} \dot{r} \quad (6.9)$$

The identification of the hydrodynamic coefficients in Eqs. 6.8-6.9 is performed similarly to the previous case. The times series of measurements of Y_{meas} , N_{meas} , ur , $r|r|$, and \dot{r} are arranged as column vectors, and a new matrix $R = [\vec{ur}, \vec{r|r|}, \vec{\dot{r}}]$ is created. The hydrodynamic coefficients are estimated

$$[Y_{ur}^* \ Y_{rr} \ Y_{\dot{r}}]^T = R^\dagger \vec{Y}_{\text{meas}} \quad (6.10)$$

$$[N_{ur}^* \ N_{rr} \ N_{\dot{r}}]^T = R^\dagger \vec{N}_{\text{meas}} \quad (6.11)$$

where $R^\dagger := (R^T R)^{-1} R^T$ is the pseudo-inverse of non-square matrix R .

6.1.3 Pure-Surge

Estimation of coefficients X_{uu} and $X_{\dot{u}}$ is based on measurement of surge force X in the *pure-surge* VPMM maneuver, where the craft is prescribed only a time varying surge velocity $u(t)$ equal to the design velocity u_o plus a small sinusoidal perturbation with amplitude $0.02u_o$ and frequency 0.667Hz . The effects of sway and yaw are nonexistent here, so control surfaces should not be removed for this maneuver as to avoid measuring excess drag from the sockets of missing rudders. Instead, control surfaces are present and locked at zero-degrees. For the pure-surge VPMM test, AUV dynamics (Eq. 6.1) simplify to

$$X_{\text{meas}} = X_{uu} u|u| + X_{\dot{u}} \dot{u} \quad (6.12)$$

where X_{meas} is the measured surge-force. From a *single* times series of measurements, datapoints of X_{meas} , $u|u|$, and \dot{u} are arranged as column vectors, and a new matrix $U = [\vec{u|u|}, \vec{\dot{u}}] \in \mathbb{R}^{n \times 2}$ is created. Hydrodynamic coefficients are estimated:

$$[X_{uu} \ X_{\dot{u}}]^T = U^\dagger \vec{X}_{\text{meas}} \quad (6.13)$$

where $U^\dagger := (U^T U)^{-1} U^T$ is the pseudo-inverse of non-square matrix U .

6.1.4 VPMM Computational Setup

The VPMM computational meshes contain approximately 3 million cells each, with each element connected to the hull surface being approximately 0.2 percent the hull length. Shown in Figure 6.6 is a cross section of VPMM mesh cells near the surface of the hull:

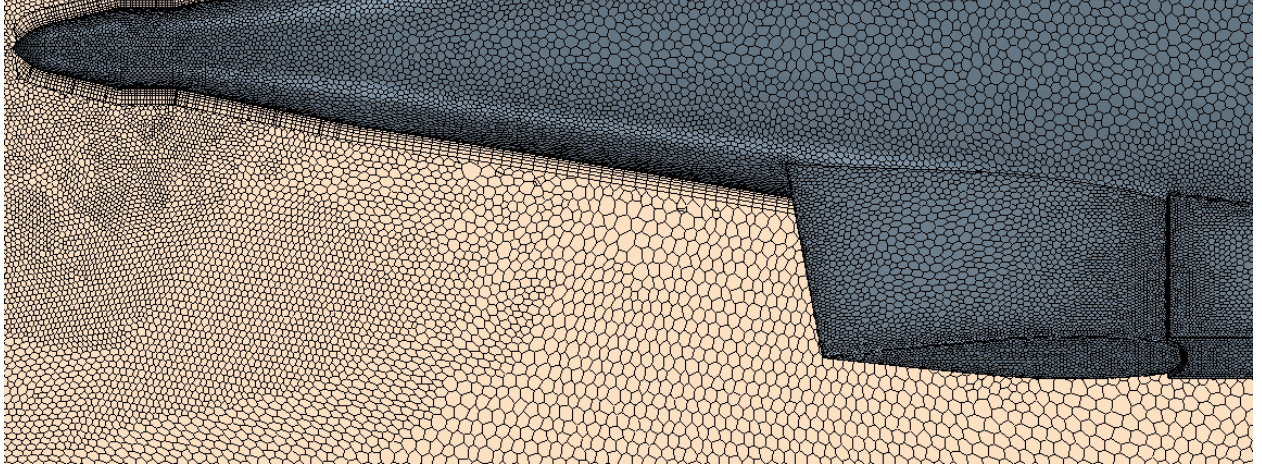


Figure 6.6 – CELL DENSITY NEAR THE AUV TAIL FOR A VPMM TEST.

Even finer meshes of 12 million cells were considered, and it was witnessed that meshes with 3 million cells saw no decrease in accuracy. The VPMM meshes are unstructured and highly refined around the hull, with 12 prism layers to capture boundary layer growth and separation and resolve vorticity shed in the near-field. The computational domain extends 15m ahead of the craft's starting position.

Our particular VPMM setup uses an inner moving mesh within the computational domain to emulate the planar motion trajectory, which requires the domain to extend far ahead of the craft for clearance. This approach is necessary for the pure surge maneuver, but is not required for the pure sway or pure yaw maneuvers, where it is possible to assign a fluid inflow velocity to the entire computational domain instead of having the hull physically move forward within the domain.

6.2 Estimation of Rudder Control Surface Coefficients

Control surface coefficients are estimated through virtual steady towing tests, with hull attack angle $\beta = r = v = 0$ and a constant vehicle surge velocity u . Virtual towing tests use the same computational cell density as the VPMM tests but do not require a moving mesh. Coefficients $N_{uu\delta_r}$, $Y_{uu\delta_r}$ and $X_{uu\delta\delta}$ are derived by analyzing N_{meas} , Y_{meas} , and X_{meas} at various constant rudder angles δ_r . For each virtual towing test, AUV dynamics (Eqs. 6.1-6.3) simplify significantly, such that the following must be satisfied:

$$X_{\text{meas}} = X_{uu}u|u| + X_{uu\delta\delta}u|u|\delta_r^2, \quad X_{uu\delta\delta} < 0 \quad (6.14)$$

$$Y_{\text{meas}} = Y_{uu\delta_r}u|u|\delta_r, \quad Y_{uu\delta_r} > 0 \quad (6.15)$$

$$N_{\text{meas}} = N_{uu\delta_r}u|u|\delta_r, \quad N_{uu\delta_r} < 0 \quad (6.16)$$

The coefficient $X_{uu\delta\delta}$ is derived through evaluating $(X_{\text{meas}} - X_{uu}u|u|)$ at 0, 10, and 20-degree rudder angles. The resulting $X_{uu\delta\delta}u|u|\delta_r^2$ is then fitted to a square curve with respect to δ_r . The fitting is shown in Fig. 6.7. Coefficient $X_{uu\delta\delta}$ is always negative, measured in $\text{N}/(\text{rad}^2 \cdot (\text{m/s})^2)$.

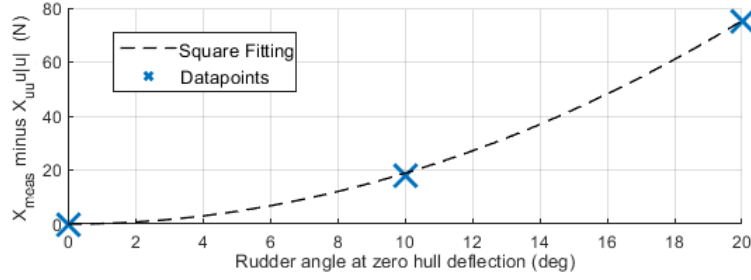


Figure 6.7 – FITTING OF $X_{UU\delta\delta}U|U|\delta_R^2$ VIA MULTIPLE CFD TOWING TESTS. Y-AXIS INVERTED FOR VISUAL CLARITY.

Similarly, the coefficient $Y_{uu\delta_r}$ is derived through analyzing the *linear* relationship between Y_{meas} and δ_r at $\delta_r = 0, 10$, and 20 -degrees, as shown in Fig. 6.8. $Y_{uu\delta_r}$ is equivalent to the slope divided by $u|u|$, and is always positive, measured in $\text{N}/(\text{rad} \cdot (\text{m/s})^2)$.

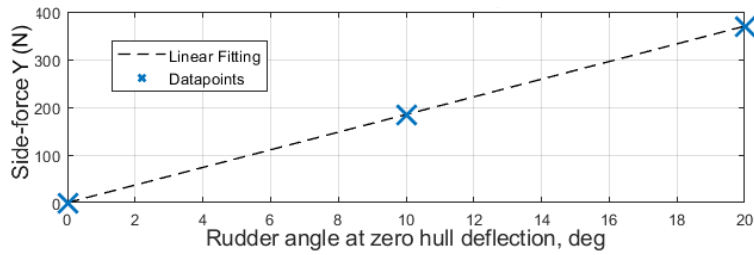


Figure 6.8 – FITTING OF $Y_{UU\delta_R}U|U|\delta_R$ VIA MULTIPLE CFD TOWING TESTS.

Likewise, $N_{uu\delta_r}$ is derived through analyzing N_{meas} about the center of buoyancy with respect to δ_r at $\delta_r = 0, 10$, and 20 -degrees, shown in Fig. 6.9. $N_{uu\delta_r}$ is equivalent to the slope divided by $u|u|$ and is always negative for rear fins, measured in $(\text{N}\cdot\text{m})/(\text{rad} \cdot (\text{m/s})^2)$.

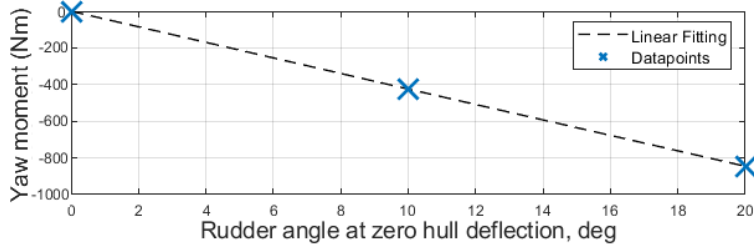


Figure 6.9 – FITTING OF $N_{UU\delta_R}U|U|\delta_R$ VIA MULTIPLE CFD TOWING TESTS.

6.3 Vertical Plane (Pitch-Axis) Coefficients

Coefficients related to the vertical plane are derived in a similar manner to those in the horizontal plane. With the same CFD setup, the craft is rotated 90° , and the same maneuvers are run on a (now vertical) plane.

6.3.1 Pitch-Axis Hull Coefficients

If the craft is symmetric along its pitch and yaw axes, the pitch-axis hull coefficients can be trivially estimated from their corresponding yaw-axis coefficients:

$$\begin{aligned} & [Z_{uw}, Z_{ww}, Z_{\dot{w}}, M_{uw}^*, M_{ww}, M_{\dot{w}}, Z_{uq}^*, Z_{qq}, Z_{\dot{q}}, M_{uq}^*, M_{qq}, M_{\dot{q}}] \\ & = [Y_{uv}, Y_{vv}, Y_{\dot{v}}, -N_{uv}^*, -N_{vv}, -N_{\dot{v}}, -Y_{ur}^*, -Y_{rr}, -Y_{\dot{r}}, N_{ur}^*, N_{rr}, N_{\dot{r}}] \end{aligned} \quad (6.17)$$

Otherwise, the craft must be listed 90°, and the *pure-sway* and *pure-yaw* VPMM trials must be re-run. Coefficients $[Z_{uw}, Z_{ww}, Z_{\dot{w}}, M_{uw}^*, M_{ww}, M_{\dot{w}}, Z_{uq}, Z_{qq}, Z_{\dot{q}}, M_{uq}^*, M_{qq}, M_{\dot{q}}]$ are equivalent to new values $[Y_{uv}, Y_{vv}, Y_{\dot{v}}, -N_{uv}^*, -N_{vv}, -N_{\dot{v}}, -Y_{ur}^*, -Y_{rr}, -Y_{\dot{r}}, N_{ur}^*, N_{rr}, N_{\dot{r}}]$ estimated from the new 90°-listed VPMM trials.

6.3.2 Elevator Control Surface Coefficients

If the control surfaces of the craft are symmetric along its pitch and yaw axes, the elevator control surface coefficients can be trivially estimated from their corresponding rudder coefficients:

$$\begin{bmatrix} Z_{uu\delta e} \\ M_{uu\delta e} \end{bmatrix} = \begin{bmatrix} Y_{uu\delta r} \\ -N_{uu\delta r} \end{bmatrix} \quad (6.18)$$

Otherwise, the craft must be listed 90° and the virtual steady towing tests must be re-run. Coefficients $(Z_{uu\delta e}, M_{uu\delta e})$ are equivalent to new values $(Y_{uu\delta r}, -N_{uu\delta r})$ that were estimated from the new 90°-listed virtual steady towing tests.

6.3.3 Canard Control Surface Coefficients

Canard control surface coefficients $X_{uu\delta\delta_c}$, $Z_{uu\delta_c}$, and $M_{uu\delta_c}$ are derived in a manner similar to that of $X_{uu\delta\delta}$, $Y_{uu\delta r}$, and $N_{uu\delta r}$, respectively. As with the rear control surfaces, the force along \hat{x} resulting from canard deflection angle δ_c scales with the square of the deflection angle. Therefore, the method for estimating the coefficient $X_{uu\delta\delta_c}$ is identical to that of the coefficient $X_{uu\delta\delta}$, except instead of the datapoints $\delta_r = 0, 10$, and 20-degrees, the datapoints $\delta_c = 0, 10$, and 20-degrees are tested on the canards. As with $X_{uu\delta\delta}$, the coefficient $X_{uu\delta\delta_c}$ is always negative.

Likewise, the force Z and moment M resulting from canard deflection scale linearly with canard angle δ_c , making the estimation of coefficients $Z_{uu\delta_c}$ and $M_{uu\delta_c}$ practically identical to the estimation of coefficients $Y_{uu\delta r}$ and $N_{uu\delta r}$, respectively. The datapoints $\delta_c = 0, 10$, and 20-degrees are tested in a virtual towing tank environment, and a regression line is constructed. For front canards, coefficient $Z_{uu\delta_c}$ is always negative, and coefficient $M_{uu\delta_c}$ is always positive.

6.4 Roll Coefficients

6.4.1 Estimation of Control Surface Roll Coefficient $K_{uu\delta_{roll}}$

If the average radial distance x_F between the roll-axis of the hull and center of pressure of the rudders is known, $K_{uu\delta_{roll}}$ can be approximated as

$$K_{uu\delta_{roll}} \approx -2Y_{uu\delta r}x_F \quad (6.19)$$

Otherwise, another virtual towing-tank test must be run, with all control fins equally deflected clockwise in accordance with Figure 3.4. The roll moment K is measured at various δ_{roll} commands. $K_{uu\delta_{roll}}$ is derived through analyzing the linear relationship between roll moment K_{meas} and δ_{roll} at $\delta_{roll} = 0^\circ, 10^\circ$, and 20° , as shown in Fig. 6.10. $K_{uu\delta_{roll}}$ is equivalent to the slope divided by $u|u|$, and is always negative, measured in $(N\cdot m)/(rad \cdot (m/s)^2)$.

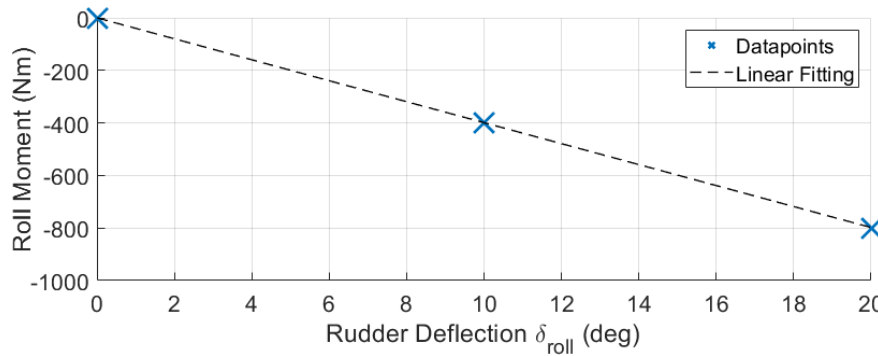


Figure 6.10 – FITTING OF $K_{uu\delta_{ROLL}}$ VIA MULTIPLE CFD TOWING TESTS.

6.4.2 Estimation of Hull Coefficients K_{up} , K_{pp} , and $K_{\dot{p}}$

As a first approximation, the coefficients (K_{up} , K_{pp} , $K_{\dot{p}}$) which represent the hydrodynamic resistance to roll can be approximated using sway coefficients originally obtained from the virtual *pure-sway* maneuver. For a symmetric vehicle in sway, the roll moment on the isolated top half of the craft should be approximately half the total sway force multiplied by some moment-arm. The use of a moment-arm implies the moment can be generated with a virtual point-force. The location of this point-force is assumed to be near the outer radius of the craft, as the point-torque distribution should naturally increase with radial distance (leverage). For a ballpark estimate, we simply place the moment-arm on the effective outer radius x_R of the hull. The isolated roll-moment from the top half of a craft in sway is then approximated as half the total sway force multiplied by the craft's outer radius.

In context, we understand that a roll-induced virtual sway is also occurring in the tangential plane, where the overall magnitude of roll moment K can be reconstructed from two separate tangential projections on the separate planes. Furthermore, the magnitude of side-slip velocity across the entire skin of a rolling vehicle is its effective radius x_R multiplied by the roll rate p . The roll moment can therefore be estimated as four times the moment from the isolated top half of the vehicle in sway, where the *sway* is actually a virtual side-slip velocity induced by roll. The roll coefficients K_{up} , K_{pp} , and $K_{\dot{p}}$ are then roughly approximated as

$$\begin{aligned} K_{up} &\approx 2 x_R^2 Y_{uv} \\ K_{pp} &\approx 2 x_R^2 Y_{vv} \\ K_{\dot{p}} &\approx 2 x_R^2 Y_{\dot{v}} \end{aligned} \tag{6.20}$$

For a typical roll-stable craft which is not expected to roll considerably, it is only important that K_{up} , K_{pp} , and $K_{\dot{p}}$ are the correct sign and relative order of magnitude to achieve full modeling accuracy. Further refinement of the roll coefficients appears to have a non-existent or negligible role in simulation accuracy when within the correct order of magnitude. Therefore, for the majority of AUVs and submersibles, roll coefficient approximation via Equation (6.20) is adequate.

For the highest achievable roll accuracy, especially for craft intended to adopt roll control, a more thorough CFD-based approach can be taken to obtain accurate values for the coefficients K_{up} , K_{pp} , and $K_{\dot{p}}$. These three coefficients can be accurately identified from the *pure-roll* virtual motion maneuver. This maneuver operates with a constant surge inflow velocity u_o , where a sinusoidal roll rotation is also prescribed. The roll rotation amplitude is chosen to be 10° at a frequency of 0.667Hz. CFD mesh refinement is similar to the mesh used the VPMM maneuvers, but the computational domain does not need to extend as far ahead of the craft, as a constant inflow velocity can be assigned without the craft progressing in position along \hat{x} . For the pure-roll motion mechanism test, relevant AUV dynamics simplify to:

$$K_{\text{meas}} = K_{up}up + K_{pp}p|p| + K_{\dot{p}}\dot{p} \tag{6.21}$$

where K_{meas} is the measured roll-moment. From a single times series of measurements, datapoints of K_{meas} , up , $p|p|$, and \dot{p} are arranged as column vectors, and a new matrix $P = [\vec{up}, \vec{p|p|}, \vec{\dot{p}}]$ is created. Hydrodynamic coefficients are estimated:

$$[K_{up} \ K_{pp} \ K_{\dot{p}}]^T = P^\dagger \vec{K}_{\text{meas}} \tag{6.22}$$

where $P^\dagger := (P^T P)^{-1} P^T$ is the pseudo-inverse of non-square matrix P .

7. 6-DOF MODEL SIMULATION AND CONSTRUCTION

7.1 Open-Loop Simulation

An open-loop simulation is presented in Figure 7.1.

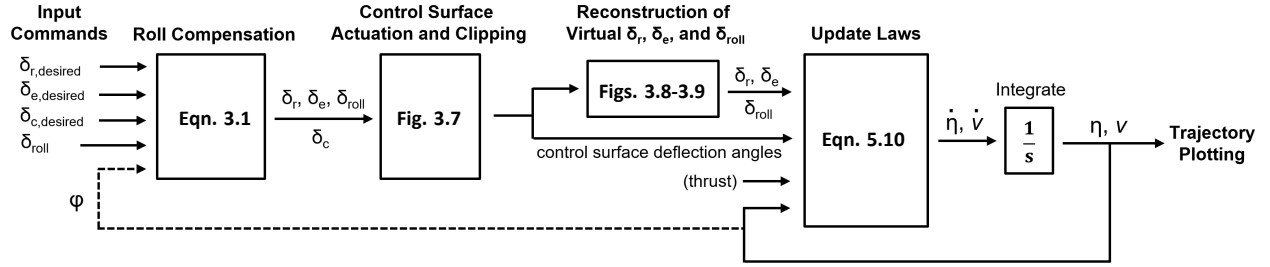


Figure 7.1 – FULL 6-DOF OPEN-LOOP SIMULATOR LAYOUT.

For the open-loop 6-DOF simulation, trajectory is plotted for rudder angle $\delta_r = 10^\circ$ at launch velocity $u_o = 2\text{m/s}$ in Figure 7.5, over the course of 200 seconds. For visualization purposes, the \hat{z} and \hat{y} -axes are now flipped such that \hat{z} is oriented upwards. The craft is given a constant thrust equal to $-X_{uu}u_o^2$. During this turning-circle simulation, the craft evidently drifts upwards against gravity due to its 0.2% prescribed positive buoyancy.

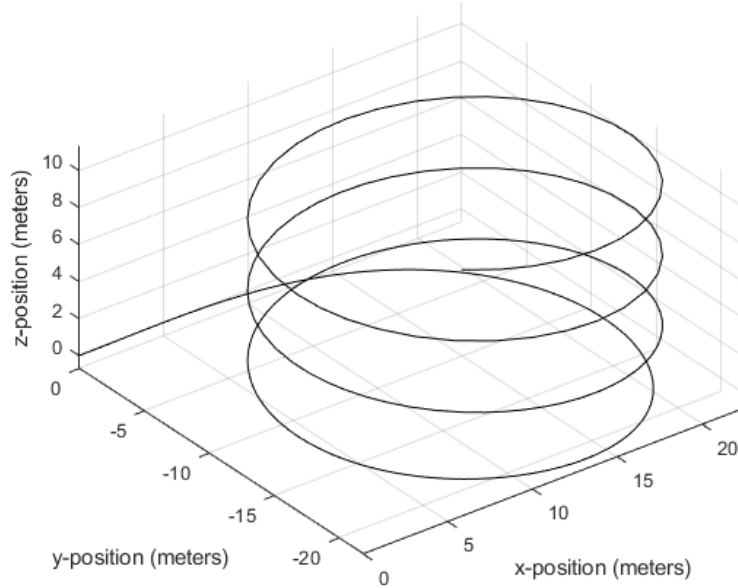


Figure 7.2 – FULL 6-DOF OPEN-LOOP SIMULATOR TRAJECTORY OUTPUT.

7.2 Closed-Loop Simulation

By making a desired rudder command δ_{roll} , δ_e , or δ_r proportional to corresponding world frame orientations ϕ , θ , or ψ , respectively, closed-loop control can be achieved straightforwardly. Implementation of unity feedback in the yaw-axis, for example, is achieved by making the desired rudder command δ_r proportional to the negative of the difference between the yaw orientation ψ and a reference orientation ψ_{ref} , shown in Figure 7.3.

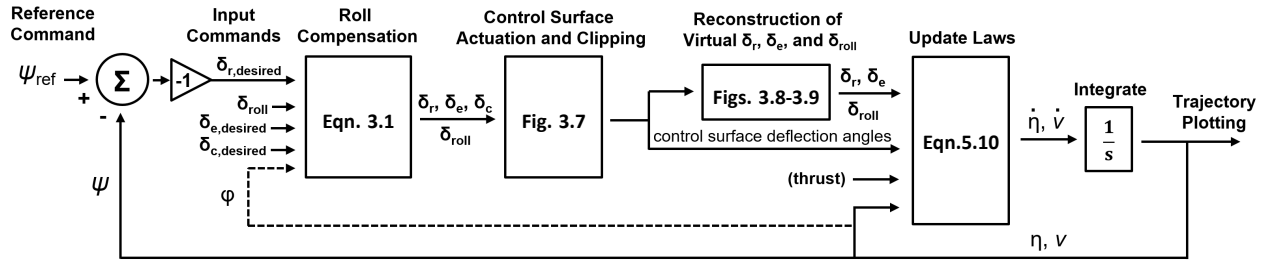


Figure 7.3 – FULL 6-DOF UNITY-FEEDBACK (YAW) CLOSED-LOOP SIMULATOR.

Rudder angle δ_r is made proportional to the *negative* of the difference between the yaw orientation ψ and a reference yaw orientation ψ_{ref} , because by convention (Figure 2.2), positive δ_r induces a negative moment about \hat{z} (i.e. $N_{uu\delta_r} < 0$). The same inverse proportionality applies for roll control ($K_{uu\delta_{roll}} < 0$), but not for pitch-axis control ($M_{uu\delta_e}, M_{uu\delta_c} > 0$). A yaw controller C_ψ is implemented for horizontal-axis control, shown in Figure 7.4.

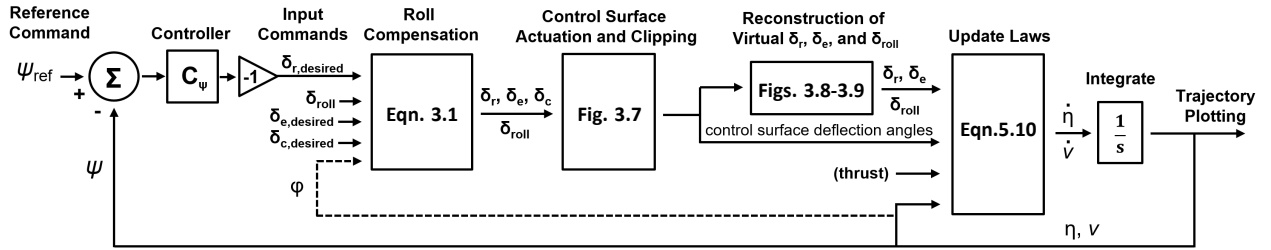


Figure 7.4 – FULL 6-DOF CLOSED-LOOP SIMULATOR WITH YAW-CONTROL.

With basic proportional feedback implemented on yaw ($C_\psi = 5$), trajectory is plotted for $\psi_{ref} = 10^\circ$ at launch velocity $u_o = 2\text{m/s}$ in Figure 7.5 over the course of 70 seconds:

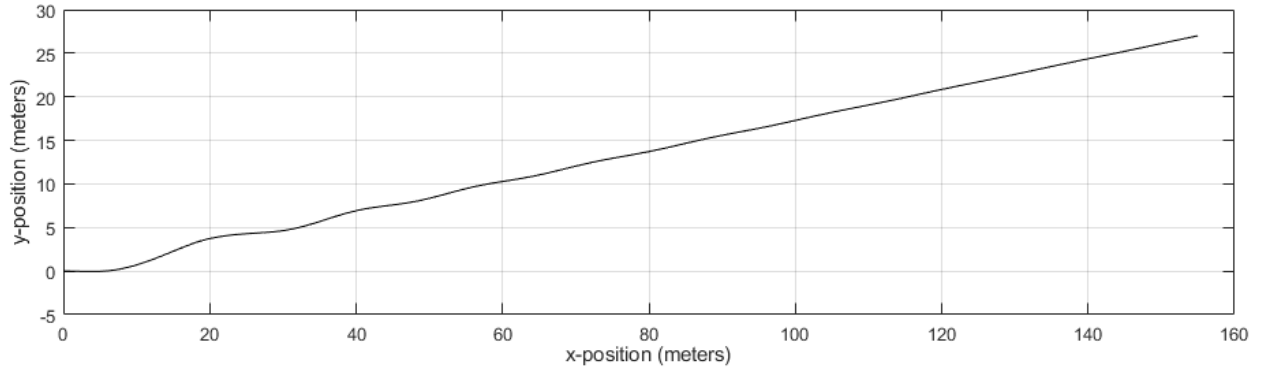


Figure 7.5 – FULL 6-DOF CLOSED-LOOP SIMULATOR TRAJECTORY WITH SIMPLE PROPORTIONAL FEEDBACK IN YAW.

8. Accuracy Assessment Using VT-690 AUV CFD Trajectory

To gauge model performance, trajectories of the VT-690 AUV during steady-state turning-circle CFD maneuvers are compared against their equivalent 6-DOF model trajectories. Turning-circle maneuvers can be used to easily validate or compare accuracy between different model types and are thereby used for all free-trajectory simulations covered in this study. In any turning-circle maneuver, the vehicle is given an initial velocity $u_o = 2.06\text{m/s}$ in surge, with a constant thrust equivalent to $-X_{uu}u_o^2$ and a constant nonzero rudder deflection δ_r . Our particular turning-circle CFD setup is deemed sufficient to serve as an adequate reference for accuracy, with a cylindrical computational domain containing approximately 3-million cells.

8.1 Full CFD Turning-Circle Model

In a CFD turning-circle simulation, the vehicle resides in the center of the domain, which has a radius of 100m and a height of 60m. Mesh settings such as prism layer settings and cell sizes are generally consistent between the CFD circular maneuvers and VPMM tests. Each element contacting the hull is set to be approximately 0.2% the vehicle length, with wake refinement applied up to one vehicle length behind the craft. The computational setup contains 12 prism layers for a boundary $y^+ \approx 1$, ensuring accurate flow development between time-steps. The fluid turbulent kinetic energy along the wake of a craft during a CFD turning-circle simulation is shown in Fig. 8.1 for $\delta_r = 20^\circ$.

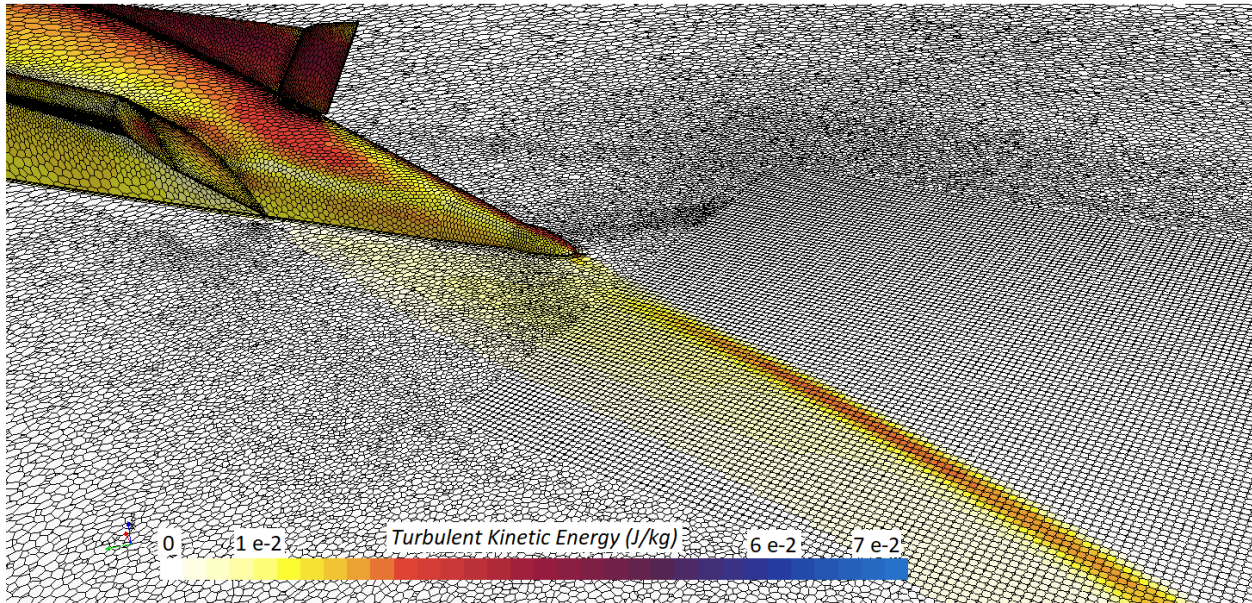


Figure 8.1 – CFD TURNING MANEUVER SIMULATION WITH 20-DEGREE RUDDER DEFLECTION.

8.2 6-DOF Model Trajectory Comparison

Three tests were conducted for assessing steady-state turning with 10, 15, and 20-degree rudder deflections to gauge the 6-DOF simulation accuracy for the VT-690. A comparison of steady-state turning-radii is presented in Table 8.1.

Table 8.1 – VT-690 TURNING-CIRCLE MANEUVER RADII IN LENGTHS L

	$\delta = 10^\circ$	$\delta = 15^\circ$	$\delta = 20^\circ$
StarCCM+ DFBI CFD Model	6.23 L	4.35 L	3.88 L
6-DOF Mathematical Model	5.43 L	3.96 L	3.16 L
Error	0.80 L	0.39 L	0.72 L

Likewise, Table 8.2 compares the CFD turning-circle steady-state drift-angles of the VT-690 against results from the 6-DOF mathematical model.

Steady-state surge velocity u is compared for the VT-690 turning-circle maneuvers in Table 8.3.

Table 8.2 – VT-690 TURNING-CIRCLE MANEUVER HULL DRIFT ANGLES

	$\delta = 10^\circ$	$\delta = 15^\circ$	$\delta = 20^\circ$
StarCCM+ DFBI CFD Model	3.42°	4.73°	5.58°
6-DOF Mathematical Model	3.98°	5.11°	6.05°
Error	0.56°	0.38°	0.47°

Table 8.3 – VT-690 PERCENT DECREASE IN STEADY-STATE SURGE VELOCITY FROM U_O

	$\delta = 10^\circ$	$\delta = 15^\circ$	$\delta = 20^\circ$
StarCCM+ DFBI CFD Model	6.060%	10.920%	15.731%
6-DOF Mathematical Model	5.574%	8.393%	13.253%
Error	0.486%	2.527%	2.478%

For the large X-tail Concept AUV, two more tests were conducted to assess steady-state turning accuracy with rudder deflected 10° and 20° . Table 8.4 compares CFD turning-circle radii of the large virtual craft against the equivalent 6-DOF LPM simulations.

Table 8.4 – X-TAIL AUV TURNING-CIRCLE RADII IN LENGTHS L

	$\delta = 10^\circ$	$\delta = 20^\circ$
StarCCM+ DFBI CFD Model	5.78 L	3.49 L
6-DOF Mathematical Model	6.22 L	3.86 L
Error	0.44 L	0.37 L

Table 8.5 compares the CFD turning-circle steady-state drift-angles of the large virtual craft against the equivalent 6-DOF LPM simulations.

Table 8.5 – X-TAIL AUV TURNING-CIRCLE HULL DRIFT ANGLES

	$\delta = 10^\circ$	$\delta = 20^\circ$
StarCCM+ DFBI CFD Model	8.65°	13.21°
6-DOF Mathematical Model	7.72°	12.19°
Error	0.93°	1.02°

Lastly, steady-state surge velocity u is compared for each X-tail AUV turning-circle maneuver in 8.6.

Table 8.6 – X-TAIL AUV PERCENT DECREASE IN STEADY-STATE SURGE VELOCITY FROM U_O

	$\delta = 10^\circ$	$\delta = 20^\circ$
StarCCM+ DFBI CFD Model	6.060%	15.731%
6-DOF Mathematical Model	5.574%	13.253%
Error	0.486%	2.478%

9. CONCLUSION

This study thoroughly detailed the complete construction of a six-DOF dynamic AUV model which performs at a relatively high level of accuracy [18, 4]. From first-principals, we thoroughly discussed and derived all aspects of that model, with general guidelines and information on avoiding redundancies, from control-command implementation to 6-DOF simulation. Uncertainties in the literature regarding VPMM such as frequency and coefficient redundancy were clarified. The six-DOF model was shown to work well for the particular AUVs used in validation, though all aspects of this study were intentionally made generic such that the simulation performance is expected to be similar for any torpedo-profiled underwater vehicle of any size or control-surface configuration.

SYMBOLS AND ABBREVIATIONS

α	Vehicle drift angle (heading - orientation) about the pitch-axis
AoA	Angle of Attack
AUV	Autonomous Underwater Vehicle
b	Buoyant displacement
β	Vehicle drift angle (heading - orientation) about the yaw-axis
CAD	Computer-Aided Design
$C_A(\nu)$	Six-DOF hydrodynamic added-Coriolis matrix
$C_{RB}(\nu)$	Six-DOF rigid-body Coriolis matrix
C_G	Center of Gravity
CFD	Computational Fluid Dynamics
$D(\nu)$	Six-DOF hydrodynamic damping Matrix
DOF	Degree(s) of Freedom
δ_c	Virtual pitch-elevator command for canards
δ_e	Virtual pitch-elevator command for rear fins
δ_r	Virtual yaw-rudder command for rear fins
δ_{roll}	Virtual roll command for rear fins
δ_i	Physical angular deflection of a control-surface with index i
EOM	Equations(s) of Motion
η	World-frame position vector $[x, y, z, \phi, \theta, \psi]^T$
Γ_i	Static alignment angle (about roll axis) of a control-surface with index i
$G(\eta)$	Six-DOF force vector of gravitational restoring forces and moments
i	Index
$I_{(ij)}$	Moment of inertia about (ij)
K	Body-frame roll-moment
K_{meas}	Hydrodynamic roll moment measured during a CFD maneuver
$K_{(subscript\ of\ variables)}$	Sub-component of roll moment K which multiplies the product of all elements in the specified <i>subscript</i>
L	Length
LPM	Lumped-Parameter Model
M	Body-frame pitch-moment
m	Mass
$M_{(subscript\ of\ variables)}$	Sub-component of pitch moment M which multiplies the product of all elements in the specified <i>subscript</i>
M_{RB}	Six-DOF rigid-body mass matrix
M_A	Six-DOF hydrodynamic added-mass matrix

N	Body-frame yaw-moment
N_{ext}	External yaw moment acting on the body
n	Number of timesteps in an unsteady CFD simulation
n	Total number of rear control surfaces
n_e	Number of rear control surfaces that are not positioned at $\Gamma_i = \frac{\pi}{2}$ or $\Gamma_i = \frac{3\pi}{2}$
n_r	Number of rear control surfaces that are not positioned at $\Gamma_i = 0$ or $\Gamma_i = \pi$
N_{meas}	Hydrodynamic yaw moment measured during a CFD maneuver
$N_{(\text{subscript of variables})}$	Sub-component of yaw moment N which multiplies the product of all elements in the specified <i>subscript</i>
ν	Body-frame motion-states vector $[u, v, w, p, q, r]^T$
ϕ	World-frame roll orientation angle
PMM	Planar-Motion Mechanism
p	Body-frame roll rotation rate
P	Matrix composed of time-series velocity-states column vectors arranged: $[\overrightarrow{u p}, \overrightarrow{p p}, \overrightarrow{p}]$
P^\dagger	Pseudo-inverse of non-square matrix P , equal to $(P^T P)^{-1} P^T$
ψ	World-frame yaw orientation angle
ψ_{ref}	Desired world-frame heading on the horizontal plane
q	Body-frame pitch rotation rate
r	Body-frame yaw rotation rate
R	Matrix composed of time-series velocity-states column vectors arranged: $[\overrightarrow{u r}, \overrightarrow{r r}, \overrightarrow{r}]$
R^\dagger	Pseudo-inverse of non-square matrix R , equal to $(R^T R)^{-1} R^T$
τ	Six-DOF control force vector of all propulsion and control-surface forces
θ	World-frame pitch orientation angle
u	Body-frame surge (forward positive) velocity
u_o	Vehicle design velocity; expected cruise speed
U	Matrix composed of time-series velocity-states column vectors arranged: $[\overrightarrow{u u}, \overrightarrow{u}]$
U^\dagger	Pseudo-inverse of non-square matrix U , equal to $(U^T U)^{-1} U^T$
UUV	Unmanned Underwater Vehicle
VPMM	Virtual Planar-Motion Mechanism
v	Body-frame sway (rightward positive) velocity
V	Matrix composed of time-series velocity-states column vectors arranged: $[\overrightarrow{u v}, \overrightarrow{v v}, \overrightarrow{v}]$
V^\dagger	Pseudo-inverse of non-square matrix V , equal to $(V^T V)^{-1} V^T$
w	Body-frame (downward positive) heave
X	Body-frame surge (forward positive) force
$(x, y, z)_G$	Sub-components of the position for center of gravity

X_{ext}	External surge force acting on the body
X_{meas}	Hydrodynamic surge force measured during a CFD maneuver
$X_{(subscript\ of\ variables)}$	Sub-component of surge force X which multiplies the product of all elements in the specified <i>subscript</i>
Y	Body-frame sway (rightward positive) force
Y_{ext}	External sway force acting on the body
Y_{meas}	Hydrodynamic sway force measured during a CFD maneuver
$Y_{(subscript\ of\ variables)}$	Sub-component of sway force Y which multiplies the product of all elements in the specified <i>subscript</i>
Z	Body-frame heave (downward positive) force
$Z_{(subscript\ of\ variables)}$	Sub-component of heave force Z which multiplies the product of all elements in the specified <i>subscript</i>

REFERENCES

- [1] H. N. Arafat, D. J. Stilwell, and W. L. Neu. Development of a dynamic model of a small high-speed autonomous underwater vehicle. In *Proc. IEEE/MTS OCEANS*, 2006. doi:10.1109/OCEANS.2006.306895.
- [2] Sajjad Ardeshtari, S. Hossein Mousavizadegan, and Saeid Kheradmand. Virtual simulation of PMM tests independent of test parameters. *Brodogradnja*, 71(2):55–73, 2020. doi:10.21278/brod71204.
- [3] Ryan Coe. Virtual Planar Motion Mechanism Tests in a CFD Environment. In *Virginia Space Grant Consortium Student Research Conference*, number December, pages 1–8, Williamsburg, VA, 2014.
- [4] Suleyman Duman and Sakir Bal. Prediction of the turning and zig-zag maneuvering performance of a surface combatant with URANS. *Ocean Systems Engineering-an International Journal*, 7(4):435–460, 2017.
- [5] Bruno M Ferreira, Anibal C. Matos, and Nuno A. Cruz. Modeling and control of TriMARES AUV. 2015.
- [6] Thor I Fossen. *Guidance and Control of Ocean Vehicles*. Wiley, New York, 1994.
- [7] Thor I (NTNU) Fossen. *Handbook of Marine Craft Hydrodynamics and Motion Control*, volume 36. John Wiley & Sons Ltd, 1 edition, 2011. doi:10.1109/mcs.2015.2495095.
- [8] Jesse Stuart Geisbert. *Hydrodynamic Modeling for Autonomous Underwater Vehicles Using Computational and Semi-Empirical Methods*. PhD thesis, Virginia Tech, 2007. URL: <https://vtechworks.lib.vt.edu/bitstream/handle/10919/33195/JGeisbertThesis.pdf>.
- [9] Ehsan Javanmard, Shahriar Mansoorzadeh, and Javad A. Mehr. A new CFD method for determination of translational added mass coefficients of an underwater vehicle. *Ocean Engineering*, 215(August):107857, 2020. doi:10.1016/j.oceaneng.2020.107857.
- [10] Michael E Kepler, Suraj Pawar, Daniel J Stilwell, Stefano Brizzolara, and Wayne L Neu. Assessment of AUV Hydrodynamic Coefficients from Analytic and Semi-Empirical Methods. In *OCEANS MTS/IEEE Charleston 2018*, 2018.
- [11] E V Lewis. *Principles of Naval Architecture - Motions in waves and controllability*, volume 3. SNAME, 2 edition, 1989. URL: <http://opac.vimaru.edu.vn/edata/EBook/PrinciplesofNavalarchitecture.pdf>.
- [12] N. M. Nouri, K. Mostafapour, and R. Bahadori. An apparatus to estimate the hydrodynamic coefficients of autonomous underwater vehicles using water tunnel testing. *Review of Scientific Instruments*, 87(6), 2016. URL: <http://dx.doi.org/10.1063/1.4950899>, doi:10.1063/1.4950899.
- [13] Yu Cun Pan, Huai Xin Zhang, and Qi Dou Zhou. Numerical prediction of submarine hydrodynamic coefficients using CFD simulation. *Journal of Hydrodynamics*, 24(6):840–847, 2012. URL: [http://dx.doi.org/10.1016/S1001-6058\(11\)60311-9](http://dx.doi.org/10.1016/S1001-6058(11)60311-9), doi:10.1016/S1001-6058(11)60311-9.
- [14] Yu Cun Pan, Qi Dou Zhou, and Huai Xin Zhang. Numerical simulation of rotating arm test for prediction of submarine rotary derivatives. *Journal of Hydrodynamics*, 27(1):68–75, 2015. URL: [http://dx.doi.org/10.1016/S1001-6058\(15\)60457-7](http://dx.doi.org/10.1016/S1001-6058(15)60457-7), doi:10.1016/S1001-6058(15)60457-7.
- [15] Jong Yong Park, Nakwan Kim, and Yong Ku Shin. Experimental study on hydrodynamic coefficients for high-incidence-angle maneuver of a submarine. *International Journal of Naval Architecture and Ocean Engineering*, 9(1):100–113, 2017. URL: <http://dx.doi.org/10.1016/j.ijnaoe.2016.08.003>, doi:10.1016/j.ijnaoe.2016.08.003.
- [16] A. B. Phillips, M. Furlong, and S. R. Turnock. Virtual planar motion mechanism tests of the autonomous underwater vehicle autosub. In *CFD in Ship Design*, pages 1–8, 2007. URL: <http://eprints.soton.ac.uk/48939/>.
- [17] Timothy Timothy Jason Prestero. *Verification of a Six-Degree of Freedom Simulation Model*. PhD thesis, Massachusetts Institute of Technology, 2001. doi:10.1575/1912/3040.
- [18] Benjamin J. Racine and Eric G. Paterson. CFD-based method for simulation of marine-vehicle maneuvering. *35th AIAA Fluid Dynamics Conference and Exhibit*, (June):6–9, 2005. doi:10.2514/6.2005-4904.
- [19] Juan A. Ramírez-Macías, Persijn Brongers, Santiago Rúa, and Rafael E. Vásquez. Hydrodynamic modelling for the remotely operated vehicle Visor3 using CFD. *IFAC-PapersOnLine*, 49(23):187–192, 2016. doi:10.1016/j.ifacol.2016.10.341.

- [20] Haibin Zheng, Xin Wang, and Zebin Xu. Study on hydrodynamic performance and CFD simulation of AUV. *2017 IEEE International Conference on Information and Automation, ICIA 2017*, (July):24–29, 2017. doi:10.1109/ICInfA.2017.8078877.